energies

MDPI

Article

The Influence of the Intake Geometry on the Performance of a Four-Stroke SI Engine for Aeronautical Applications

Fabio Anaclerio [1,*], Annarita Viggiano [2,*], Francesco Fornarelli [1], Paolo Caso [3], Domenico Sparaco [3] and Vinicio Magi [2]

[1] Dipartimento di Scienze Agrarie, Alimenti, Risorse Naturali e Ingegneria, Università degli Studi di Foggia, 71122 Foggia, Italy; francesco.fornarelli@unifg.it
[2] Dipartimento di Ingegneria, Università degli Studi della Basilicata, 85100 Potenza, Italy; vinicio.magi@unibas.it
[3] Costruzioni Motori Diesel CMD S.p.A., 81020 San Nicola La Strada, Italy; paolo.caso@cmdengine.com (P.C.); domenico.sparaco@cmdengine.com (D.S.)
* Correspondence: fabio.anaclerio@unifg.it (F.A.); annarita.viggiano@unibas.it (A.V.)

Abstract: In this work, the influence of plenum and port geometry on the performance of the intake process in a four-stroke spark ignition engine for ultralight aircraft applications is analyzed. Three intake systems are considered: the so-called "standard plenum", with a relatively small plenum volume, the "V1 plenum", with a larger plenum volume, and the "standard plenum" equipped with a large curvature manifold called the "G2 port". Both measurements and 3D CFD simulations, by using Ansys® Academic Fluent, Release 20.2, are performed to characterize and analyze the steady-flow field in the intake system for selected valve lifts. The experimental data and the numerical results are in excellent agreement with each other. The results show that at the maximum valve lift, i.e., 12 mm, the V1 plenum allows an increase in the air mass flow rate of 9.1% and 9.4% compared to the standard plenum and the standard plenum with the "G2 port", respectively. In addition, the volumetric efficiency has been estimated under unsteady-flow conditions for all geometries at relatively high engine rpms. The difference between numerical results and measurements is less than 1% for the standard plenum, thus proving the accuracy of the model, which is then used to study the other configurations. The V1 plenum shows a fairly constant volumetric efficiency as the engine speed increases, although such an efficiency is lower than that of the other two geometries considered in this work. Specifically, the use of the "G2 port" leads to an increase of 1.5% in terms of volumetric efficiency with respect to the configuration with the original manifold. Furthermore, for the "G2 port" configuration, higher turbulent kinetic energy and higher swirl and tumble ratios are observed. This is expected to result in an improvement of air–fuel mixing and flame propagation.

Keywords: spark ignition engines; aeronautical propulsion; intake system; plenum geometry; port geometry; volumetric efficiency; turbulence; CFD

check for updates

Citation: Anaclerio, F.; Viggiano, A.; Fornarelli, F.; Caso, P.; Sparaco, D.; Magi, V. The Influence of the Intake Geometry on the Performance of a Four-Stroke SI Engine for Aeronautical Applications. *Energies* **2024**, *17*, 5309. https://doi.org/10.3390/en17215309

Academic Editor: Georgios Mavropoulos

Received: 28 September 2024
Revised: 17 October 2024
Accepted: 19 October 2024
Published: 25 October 2024

Copyright: © 2024 by the authors. Licensee MDPI, Basel, Switzerland. This article is an open access article distributed under the terms and conditions of the Creative Commons Attribution (CC BY) license (https://creativecommons.org/licenses/by/4.0/).

1. Introduction

Nowadays, Internal Combustion Engines (ICEs) are widespread in aeronautic, road transportation, and power generation sectors due to their high reliability. However, it is recognized that harmful emissions, i.e., CO_2, NO_x, CO, and unburned HC and particulate matter [1], occur due to the combustion process of hydrocarbon fuels. It is well known that the greenhouse gas (GHG) is the main contributor to global warming and climate-change [2]. For the aviation sector, global CO_2 emissions were estimated to be around 1.9% of the total GHG emissions in 2016, with an increase of 2.5% in 2018 [3]. Furthermore, carbon monoxide, which results from the incomplete oxidation of carbon fuel, is expected to increase with respect to the data assessed in 2020 [4]. According to the International Energy Agency (IEA), CO_2 emissions increased by 1.1% in 2023, reaching a record high of 37.4 Gt [5]. Therefore, stricter regulations have been imposed [6,7], and the use of alternative fuels [8–11] and

unconventional combustion strategies [12–14] is being investigated to meet emissions limits. In this scenario, an in-depth analysis and optimization of fluid dynamics in the combustion chamber could play a key role, leading to higher engine performance, i.e., high power with fuel consumption economy, low Cycle-to-Cycle Variability (CCV) under lean conditions, and low levels of emissions. Specifically, a well-structured in-chamber flow motion (i.e., swirl, tumble, and cross tumble), high turbulence intensity, and high volumetric efficiency are required to improve engine performance. The intake system strongly affects in-chamber fluid-dynamics, and that is why this work mainly focus on the charging process of ultralight aircraft engines.

The characterization of the intake system has been addressed by several authors by both experimental and numerical approaches. In this regard, Yang et al. [15] compared the intake port flow performance obtained with a steady-state flow bench and with 3D CFD simulations under motored conditions. The results confirmed that the steady-state measurements, in terms of discharge coefficients and swirl/tumble index, are in good agreement with motored numerical simulations. With the aim of improving the air/fuel mixing and the combustion process of a spark ignition (SI) engine, the tumble motion is investigated in detail in ref. [16] to achieve lean combustion and reduce CCV by using charge stratification, i.e., stoichiometric conditions around the spark plug and lean air/fuel mixture in the other regions. In general, high tumble levels are attained with substantial design modifications of the intake system. Li et al. [17] used a digital Particle Image Velocimetry (PIV) approach for a twin-spark ignition engine to visualize the flow field in the cylinder. The intake valves were partially shrouded with 120-degree plates to generate a high tumble and to achieve a reduction in CCV. The results show a large-scale tumble vortex at the end of the intake stroke, which stays in the chamber until the end of the compression stroke. Falfari et al. [18] used a 3D CFD solver to study the influence of intake port and manifold geometry on the tumble motion and on turbulence by varying the intake port angle (α) and the intake manifold angle (β).

Zhihua et al. [19] carried out numerical simulations under steady-state conditions to assess how different intake ports are able to generate a reverse tumble flow in a two-stroke gasoline engine. They noted that upward-facing intake ports develop a high tumble intensity at low valve lifts, whereas downward-facing intake ports give a strong tumble at high valve lifts. Wahono et al. [20] studied the influence of helical and tangential intake ports in a small motorcycle engine using both a steady-flow test rig and numerical simulations. They showed that the tangential ports are the best choice to maximize the gas velocity and to increase the in-cylinder turbulence. Lee et al. [21] proposed three intake ports geometry, with angles of 15, 20, and 25 degrees, for a four-stroke research optical engine to promote the production of a tumble flow. The influence of the tumble flow was also analyzed under lean combustion. However, high gas velocities at the end of the intake stroke usually mean a reduction in volumetric efficiency [22].

The geometry configuration of both the intake plenum and intake manifold is relevant to delivering the fresh charge into the cylinder and to control the pressure waves [23–28] through the intake port. Several studies have been carried out to investigate the influence of the intake port geometry with the aim of optimizing the in-cylinder flow field and the volumetric efficiency [29–34]. Jawand et al. [35] designed an original intake system equipped with a dual plenum configuration to separate overlapping intake processes. Steady analysis indicates that such a design increases the air mass flow rate. In addition, unsteady results show that the dual plenum intake system increases the peak pressure. Ceviz [36] experimentally investigated the influence of the intake plenum geometry on the performance of a carbureted engine in terms of engine torque, the coefficient of the variation of indicated mean effective pressure (COV_{imep}), and pulsating flow pressure in the intake manifold and emissions. Three experiments were carried out: the first experiment was conducted with the original intake manifold, whereas the second and the third experiments were with larger manifolds by adding to the original one a volume equal to 90 cm^3 and 180 cm^3, respectively. The results, obtained at speeds ranging from 1250 to 3000 rpm,

show that, at a low engine speed, the largest plenum provides an increase in pressure in the intake manifold and this improves the engine performance and reduces emissions, whereas, at high-speed regimes, a smaller plenum volume is recommended to optimize engine performance. Hamilton and Lee [34] experimentally analyzed the influence of a plenum geometry on the engine performance for several engine speeds. Their results suggest that a plenum with a larger volume strongly affects the volumetric efficiency at 9500 rpm. Specifically, a pressure peak in the plenum before the Intake Valve Opening (IVO) has been observed. Ceviz and Akin [26] studied the influence of the intake plenum length on the performance of a spark-ignition engine in terms of thermal efficiency, specific fuel consumption, brake torque, and engine power. The results show that, up to 3000 rpm, a thermal efficiency increase is observed by increasing the plenum length by 16 mm and 32 mm. From 3000 to 4000 rpm, the thermal efficiency increase occurs only for the plenum length increase of 16 mm. For much longer plenums, i.e., length increases of 48 mm and 64 mm, an opposite trend was found. Apaydin and Doner [37] carried out 3D CFD steady numerical simulations of a plenum with different profiles and diameters, i.e., 45 mm, 50 mm and 65 mm. Their optimal plenum design was the one that minimized pressure losses and provided a homogeneous velocity distribution. Pranto et al. [38] proposed three different plenum geometries (single plenum, dual plenum, and a new geometry with separator) characterized by a convergent–divergent intake duct. The investigation was carried out by using steady CFD simulations. The results show that the new geometry with the separator reduces pressure loss compared to the other two geometries.

The student Formula SAE (FSAE) standards [39] have recently introduced a restrictor to the intake system to limit the intake air flow rate. Therefore, an ad hoc plenum is generally placed before the engine intake manifold to reduce the restrictor influence, even if such a plenum increases the engine response time. Vichi et al. [40] proposed, for a four-stroke single cylinder engine, an innovative intake system to overcome the issue of increased response time. Such an intake system consists of a variable length manifold to bypass the plenum if maximum engine power is not required. The numerical simulations show that it is a good practice to bypass the plenum at low engine speeds and for throttle opening up to 60%. On the other hand, to achieve high engine performance, the intake system with the plenum gives a good compromise between performance and response time at the cost of the increased design complexity of the entire intake system. Finally, the impact of the plenum volume and runner length on engine performance has also been numerically analyzed by Venugopal and Anubhav [41], who have used 1D CFD software to optimize the design.

In this work, the intake system of a spark-ignition engine for ultralight aircrafts is studied. To the best of the authors' knowledge, this is the first attempt to optimize the intake geometry of an engine designed for aeronautical applications. Furthermore, the results in the scientific literature obtained for engines designed for ground vehicles are not yet conclusive on this subject and show that the intake geometry effect is very sensitive to the operating conditions used. Dealing with aeronautical engines, start-up, cruising, and take-off regimes are investigated in this work. Moreover, a comprehensive investigation has been carried out by using both experiments and 3D CFD numerical simulations for both steady and unsteady-flow configurations. Three different intake geometries are taken into consideration in trying to improve engine performance in terms of the volumetric efficiency and turbulence intensity of the flow field. Specifically, two plenums (standard plenum and V1 plenum) with different volumes and a new intake port geometry, named G2, are analyzed. The computational domain consists of a single cylinder together with all components of the intake system, i.e., intake air duct, plenum, manifold, and ports. A Favre-Averaged Navier–Stokes (FANS) numerical model has been used to simulate the turbulent flow field, since this model provides accurate results by using an appropriate numerical scheme and mesh resolution, as discussed in ref. [42]. Both steady numerical simulations and measurements have been performed to evaluate the mass flow rate through the intake valve for selected valve lifts and to characterize the in-cylinder flow field structure. The

investigation has also been extended to unsteady-flow configurations at different rpms, typical of aeronautical applications. The engine volumetric efficiency together with the gas temperature, composition, and turbulent kinetic energy (TKE) have been carefully analyzed. This work is organized as follows: the experimental setup and the mathematical model are first described, then the results are discussed for steady and unsteady-flow conditions, and, finally, conclusions are drawn.

2. The CMD18E Engine

A naturally aspirated four-stroke spark ignition engine for ultralight aircraft applications fueled by commercial gasoline is considered for both experiments and numerical simulations. The engine, designed by Costruzioni Motori Diesel S.p.a. and identified by the acronym CMD18E, is a Port Fuel Injection (PFI) engine with four cylinders in a boxer configuration. The engine has a Bore/Stroke (B/S) ratio equal to 1.55, a compression ratio (CR) of 10, and a total displacement equal to 1800 cc. The engine is equipped with two valves and two spark plugs per cylinder. Compared to the engine equipped with a single spark plug, the use of twin spark plugs leads to a reduction in ignition delay time, an improvement in terms of emissions due to more complete combustion, and an increase in maximum heat release, temperature, and pressure in the cylinder [43]. Moreover, it offers a significant safety advantage in the event of a failure of one of the two spark plugs. The maximum engine speed is 5800 rpm with a maximum output power of 73 kW. Table 1 summarizes the main engine specifications.

Table 1. Specifications of CMD18E engine.

Architecture	4 Cylinders Boxer
Fuel	Commercial gasoline
# valves per cylinder	2
Stroke (mm)	62
Bore (mm)	96
Compression ratio	10
Connecting rod (mm)	127
Exhaust Valve Opening (CAD)	120.45
Exhaust Valve Closing (CAD)	381.45
Intake Valve Opening (CAD)	325.45
Intake Valve Closing (CAD)	615.45

A computer-aided design view of the engine geometry, together with the baseline configuration of the intake system, is shown in Figure 1. Specifically, the figure shows the air intake section, which is located after the throttle valve, the baseline plenum, and, for each cylinder, the intake and exhaust ports and the intake and exhaust valves.

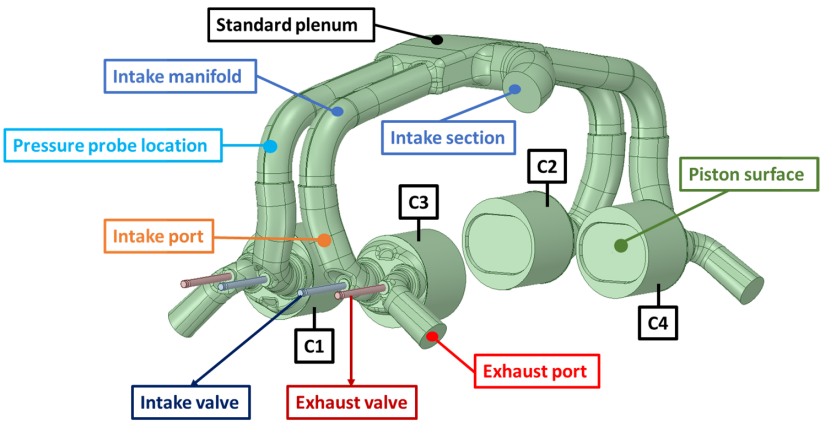


Figure 1. Computer-aided design view of the 3D engine geometry: C1, C2, C3, and C4 stand for cylinder #1, cylinder #2, cylinder #3, and cylinder #4, respectively.

Figure 2 shows the engine phase diagram as a function of the crank angle degree (CAD), whereas Figure 3 shows the exhaust and the intake valve lifts as a function of CAD, with a zero crank angle degree corresponding to TDC with combustion. The exhaust stroke ranges from 120.45 CAD to 381.45 CAD, whereas the intake valve opens at 325.45 CAD. A valve overlap of 56 CAD occurs between 325.45 CAD and 381.45 CAD.

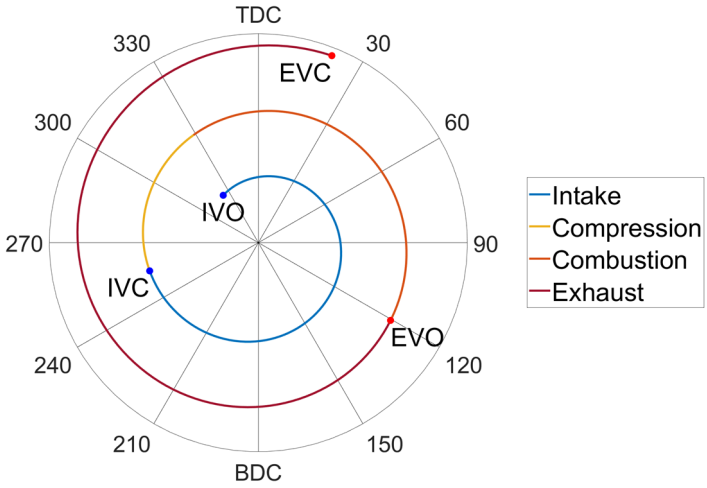


Figure 2. Phase diagram of the engine working cycle.

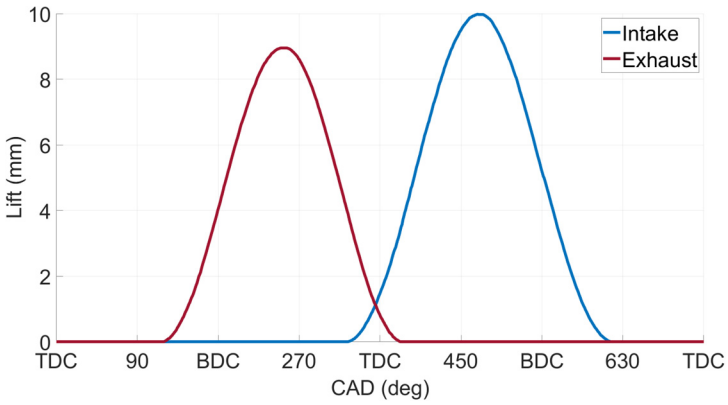


Figure 3. Exhaust and intake valve lifts as a function of CAD.

3. The Experimental Procedure

3.1. The Engine Test Bench

The experimental investigations have been carried out for the CMD18E engine with different intake systems to identify the configuration that maximizes the engine performance. A detailed layout of the engine test bench is given in Figure 4, where all the instruments are shown with the specific connections between them.

The engine is coupled with the "FR 500 BRP" eddy-current brake, which is characterized by a maximum braking power of 380 kW ranging from 2000 to 9000 rpm and a maximum torque of 1600 Nm at 2200 rpm. Additionally, the "Magnetic MA160" alternating-current motor, with nominal power equal to 120 kW, is mechanically connected to the brake system. The electric motor has been used to reach the minimum engine speed to start the warm-up procedure of the thermal engine. A single-hole injector is mounted on the intake port, and the fuel injection pressure is set to 3.8 bar.

A pressure transducer for a high-speed signal and low pressure, i.e., AVL LP12DA05, has been installed on the intake port to acquire the intake pressure of cylinder #1. A piezoelectric crystal transducer, interfaced with the Kistler 5044 and AVL X-fem U4H2, has been employed to measure the in-cylinder pressure, whereas AVL X-ion in conjunction with

AVL Indicom Software has been used to process the high-speed signals. The sensitivity of the in-cylinder pressure transducer measurements is checked at BDC ±4 CAD by comparing such data with those given from the pressure transducer mounted on the intake port of cylinder #1.

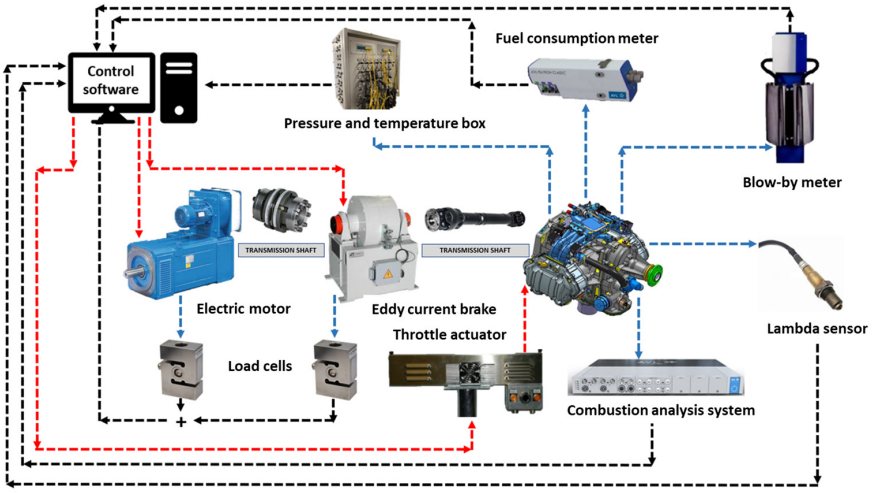


Figure 4. Layout of the engine test bench. Black dashed lines refer to input signals for post-processing; red dashed lines refer to output signals for engine control; blue dashed lines refer to engine operating conditions.

Each exhaust port has been equipped with a lambda sensor, i.e., Bosch LSU 4.9, to measure the air/fuel ratio (A/F). A comparison of this ratio with the stoichiometric A/F ratio for gasoline is made to evaluate the trapped mass of air in the cylinder. In addition, a pressure transducer suitable for low-speed signals and low-pressure conditions, the GE Unik 5000, has been used to monitor the exhaust pressure.

The fuel temperature, density, and consumption have been monitored by means of AVL PLUtron Classic. Liquid coolant temperature and air temperature in the plenum have been acquired using thermo-resistance PT100 sensors. The barometric station includes a PT100 temperature sensor together with an atmospheric pressure sensor and a relative humidity sensor.

Table 2 summarizes the specifications of the experimental instruments used along with the measurement range and the reliability and accuracy of each instrument.

Table 2. Specification of the experimental instruments.

Instrument	Model	Measured Parameter	Measurement Range	Instrument Accuracy
Eddy-current brake	FR 500 BRP	Torque power	0–1600 Nm 0–380 kW	±2 Nm ±3 kW
High-speed low-pressure transducer	AVL LP12DA05	Manifold air pressure (MAP)	0–5.0 bar	±1%
Low-speed low-pressure transducer	GE Unik 5000	Exhaust pressure	0–2.5 bar	±2%
Lambda sensor	Bosch LSU 4.9	A/F ratio	0.65–1.5	λ = 0.8: 0.8 ± 0.01 λ = 1.0: 1.016 ± 0.007 λ = 1.7: 1.7 ± 0.05
Temperature sensor	PT100	Liquid coolant and air temperature in the plenum	0–250 °C	±0.01%
Thermocouples	TC-Direct type K	Exhaust temperature	0–1100 °C	±0.01%
Fuel consumption meter	AVL PLUtron Classic	Fuel consumption	−10–100 L/h	±1%
Pressure transducer	Kistler 6052A	In-cylinder pressure	0–250.0 bar	±0.5%
Gas flow meter	Blow-by meter “AVL 442”	Blow-by flow	0.2–2.4 L/min	±1.5%
Optical Encoder	AVL 366C	Crank angle position	0–20.000	≤0.03°

Each experimental test begins with the warm-up phase, which ends once the main operating parameters (oil pressure and temperature, liquid coolant temperature, etc.) have reached stable conditions. The target rpm is achieved with linear ramps lasting 10 s, with increments occurring every 500 rpm. Then, the stabilization phase follows, during which the main engine parameters have been monitored until they stabilize before starting the data acquisition.

The duration of injection is set to obtain a slightly rich mixture ($\varphi \approx 1.1$) under Wide Open Throttle (WOT) conditions. The pressure trace has been recorded by considering 200 consecutive work cycles with a resolution equal to 0.1 CAD. All other operating parameters have been averaged over a time interval of 15 s. Furthermore, the low-speed signals (temperatures, pressures, and low-frequency analog and digital signals) have been sampled with a rate of 10 Hz. The in-cylinder pressure trace is considered reliable, and therefore acquired, if the coefficient of variance (COV) based on the indicated mean effective pressure (IMEP) is less than $\pm 3\%$.

3.2. The Air Flow Test Bench

Experimental tests have also been carried out under steady conditions to characterize the air flow structure through the intake port for different intake valve lifts. The SF-750 test bench, by SuperFlow Dynamometers & Flowbenches Company (Sussex, WI, USA), has been employed and a detailed layout of this test rig is shown in Figure 5 where the pink arrows indicate the air path.

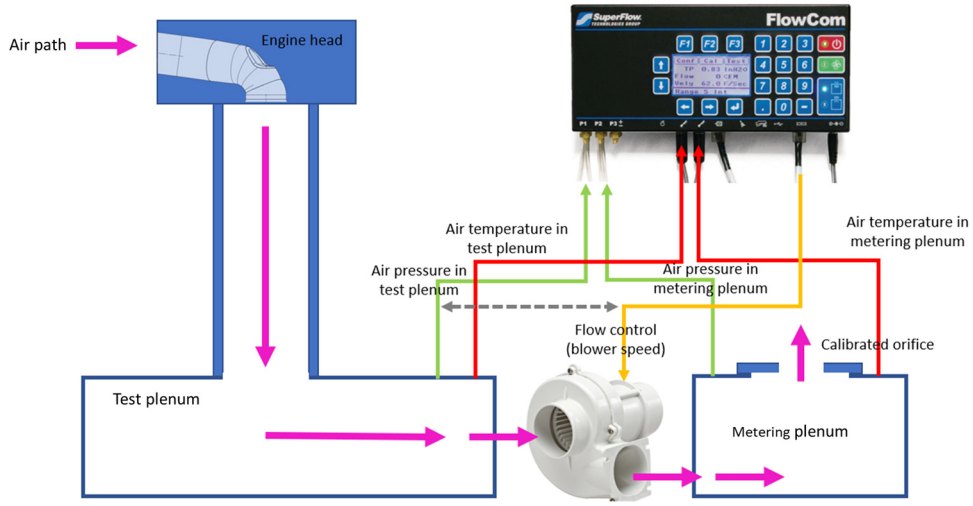


Figure 5. Layout of the SuperFlow SF-750 flow test bench. Pink arrows refer to flow air direction; red solid lines correspond to temperature signals; green solid lines refer to pressure signals; yellow line refers to blower speed control.

The flow bench consists of the CMD18E engine head, a test plenum, a blower, a metering plenum, and an electronic control unit, equipped with the FlowCom 1.0 software. A calibrated orifice is located between the metering plenum and the ambient to measure the air mass flow rate flowing through the experimental apparatus under steady conditions. The calibration has been performed based on the pressure difference between the metering plenum and the ambient.

Three pressure transducers, characterized by a measurement error of $\pm 0.5\%$, have been employed to measure the gas pressure in both the test and metering plenums and in the ambient.

In addition, gas temperature measurements are carried out by using thermistor probes with a range from -80 °C to 120 °C and with an accuracy of ± 0.3 °C. These probes are employed to measure the ambient temperature, as well as the gas temperatures, within both the test plenum and the metering plenum.

A leaking test is first performed by closing the intake valve. If a leak has been detected, the FlowCom 1.0 software subtracts the corresponding air mass flow rate from all subsequent tests. During the entire experimental campaign, the pressure inside the test plenum has been kept constant and equal to 1.062 bar. The steady tests have been performed with increments of 1 mm of the valve lift starting from 2 mm up to a maximum lift of 12 mm. For each valve lift, 10 acquisitions, each lasting one second, have been performed. Subsequently, the FlowCom 1.0 software computes both the average air mass flow rate and the corresponding measurement variability range.

4. The Mathematical Model

4.1. The Governing Equations

The governing equations are the Favre-Averaged Navier–Stokes equations for an unsteady, compressible, turbulent flow. The continuity and the momentum differential equations read as follows:

$$\frac{\partial \rho}{\partial t} + \nabla \cdot (\rho \boldsymbol{u}) = 0, \tag{1}$$

$$\rho\left(\frac{\partial \boldsymbol{u}}{\partial t} + \boldsymbol{u} \cdot \nabla \boldsymbol{u}\right) = -\nabla p + \nabla \cdot \left\{(\mu + \mu_t)\left[\nabla \boldsymbol{u} + (\nabla \boldsymbol{u})^T\right]\right\} - \nabla \cdot \left[\frac{2}{3}(\mu + \mu_t)(\nabla \cdot \boldsymbol{u})\boldsymbol{I}\right] - \nabla \cdot \left(\frac{2}{3}\rho k \boldsymbol{I}\right), \tag{2}$$

where ρ is the Reynolds averaged density, t the time, $\boldsymbol{u}$ the Favre-averaged velocity vector, p the Reynolds averaged static pressure, μ the fluid dynamic viscosity, μ_t the turbulent dynamic viscosity, $\boldsymbol{I}$ the identity matrix, and k the turbulent kinetic energy. The total internal energy differential equation is as follows:

$$\frac{\partial (\rho E)}{\partial t} + \nabla \cdot [\boldsymbol{u}(\rho E + p)] - \nabla \cdot [(\lambda + \lambda_t)\nabla T] = 0, \tag{3}$$

where E is the Favre-averaged total internal energy, λ and λ_t are the fluid and the turbulent thermal conductivity, respectively, and T is the Favre-averaged temperature. In order to evaluate the spatial distribution in the cylinder of the fresh air/fuel mixture and residual burned gas of the previous engine work cycle, two separate species are considered, i.e., fresh charge and burned gas. The two transport/diffusion equations for the mass fraction of fresh charge and burned gas are as follows:

$$\frac{\partial (\rho Y_i)}{\partial t} + \nabla \cdot (\rho \boldsymbol{u} Y_i) = -\nabla \cdot \boldsymbol{J}_i \; i = 1, 2 \tag{4}$$

where Y_i and $\boldsymbol{J}_i$ are the mass fraction and the diffusion flux of species i, respectively. In this work, both the fresh charge and burned gas species are considered as non-reacting thermally perfect gases.

A pressure-based segregated algorithm is used to numerically solve the system of the governing equations. Specifically, for unsteady numerical simulations, the Pressure Implicit with the Splitting of Operators (PISO) algorithm has been used to achieve the pressure–velocity coupling, whereas a coupled algorithm has been employed to perform steady simulations.

As regards turbulence, the standard k-ω model with shear flow corrections is employed for steady simulations. As regards unsteady simulations, the RNG k-ε model with compressibility effects is employed. This model is able to provide numerical results comparable to the experimental ones [44–46]. Standard wall functions are used to model the boundary layer near the walls. The turbulent kinetic energy and the turbulent dissipation rate (ε) equations are as follows:

$$\frac{\partial (\rho k)}{\partial t} + \nabla \cdot (\rho k \boldsymbol{u}) = \nabla \cdot [\alpha_k (\mu + \mu_t) \nabla k] + G_k + G_b - \rho \varepsilon - Y_M, \tag{5}$$

$$\frac{\partial(\rho\varepsilon)}{\partial t} + \nabla\cdot(\rho\varepsilon\boldsymbol{u}) = \nabla\cdot[\alpha_\varepsilon(\mu+\mu_t)\nabla\varepsilon] + C_{1\varepsilon}\frac{\varepsilon}{k}(G_k + C_{3\varepsilon}G_b) - C_{2\varepsilon}\rho\frac{\varepsilon^2}{k} - R_\varepsilon, \quad (6)$$

where α_k and α_ε are the inverse effective Prandtl numbers for k and ε, respectively, G_k and G_b represent the generation of k due to the mean velocity gradients and the buoyancy, respectively, Y_M is the contribution of the fluctuating dilatation in compressible turbulence to the overall dissipation rate, $C_{1\varepsilon}$, $C_{2\varepsilon}$, and $C_{3\varepsilon}$ are the model constants, and R_ε is the RNG additional term to the standard k-ε model.

Simulations were performed using Ansys® Academic Fluent software, Release 20.2.

4.2. The Computational Domain

The computational domain consists of the intake air duct, the plenum, and cylinder #1 with intake manifold and ports. Only one cylinder is considered to save computational costs. To assess the accuracy of this choice, the experimental and computed gas pressure traces in a specific location of the intake port for cylinder #1, as shown in Figure 1, are compared in Figure 6 at 5000 rpm by employing the standard plenum. As regards the computations, initially the pressure is constant throughout the intake system and equal to the value measured upstream. Therefore, an obvious difference is observed between the measured value and the assigned initial numerical value. Other than that, the slight discrepancies between measurements and numerical values suggest that some interferences with the other cylinders occur. However, the main trend is well recovered.

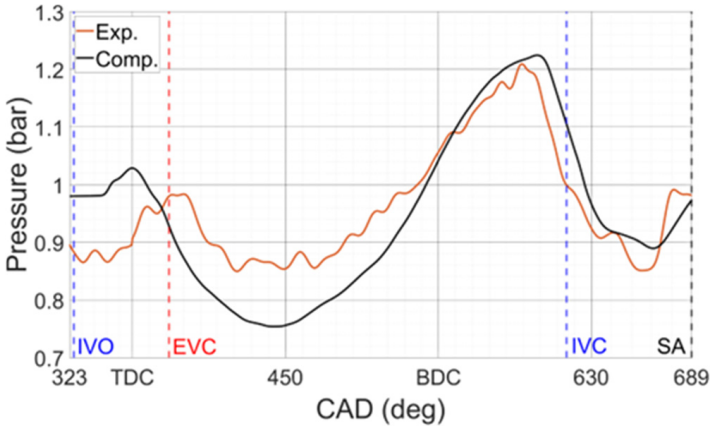
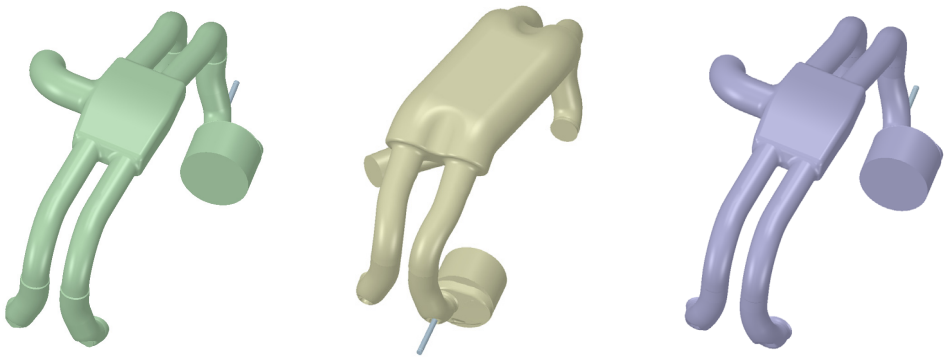


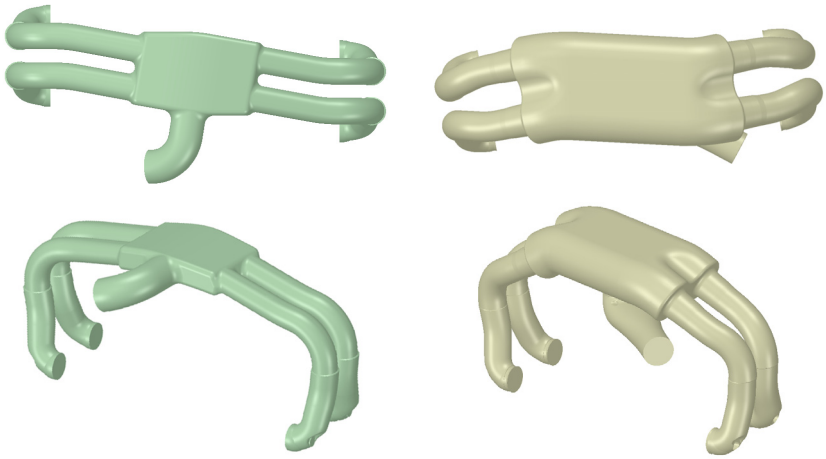
Figure 6. Experimental and numerical pressure trace in the intake port for the standard plenum at 5000 rpm.

Three different configurations, shown in Figure 7, have been analyzed and compared with the aim of optimizing the volumetric efficiency of the engine. Specifically, Figure 7a shows the baseline configuration, Figure 7b shows the plenum with a larger volume and a shorter manifold (named V1 plenum), and finally Figure 7c shows the baseline plenum with an intake manifold with a lower bend loss (named G2 port). Some other details and differences between the baseline plenum and V1 plenum are given in Figure 8. The V1 plenum volume is about 3.8 times the standard plenum volume. Furthermore, Figure 8 shows the position of the intake ducts, which allow the air to flow inside the plenums. To guarantee that air undergoes a 180-degree rotation before entering into the intake manifold in both configurations, cylinder #1 is considered for the baseline plenum and cylinder #2 for the V1 plenum configuration. A geometrical comparison between the intake manifolds of both the baseline and the V1 plenum and of the G2 port configuration is shown in Figure 9. The G2 duct is characterized by a larger radius of curvature with respect to the baseline and V1 configurations in order to decrease the bend losses, with a consequent reduction in the pressure drop due to flow deflection. Table 3 shows the geometrical specifications of the three intake systems normalized with respect to the standard plenum.



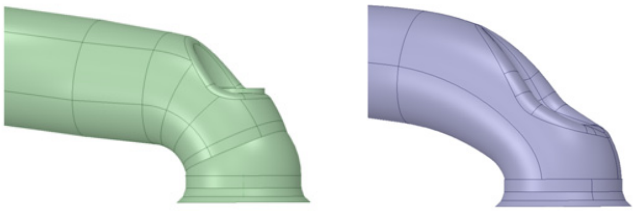
(**a**) (**b**) (**c**)

Figure 7. Rendering of the three intake configurations: (**a**) baseline (standard plenum), (**b**) V1 plenum, and (**c**) standard plenum with G2 port.



(**a**) (**b**)

Figure 8. Rendering of the standard plenum (**a**) and V1 plenum (**b**).



(**a**) (**b**)

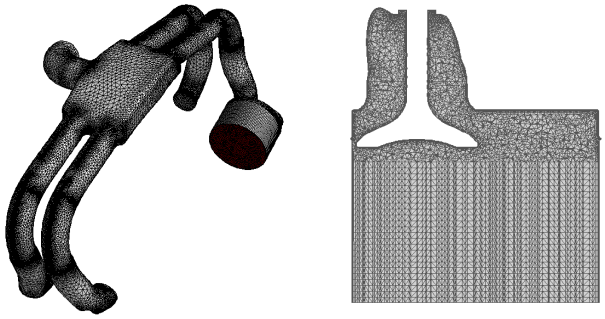
Figure 9. A detail of the baseline and V1 manifold (**a**) and G2 port (**b**).

Table 3. Geometrical specifications of the three intake systems normalized with respect to the standard plenum.

Intake System	Normalized Intake Port Diameter	Normalized Intake Port Length	Normalized Plenum Volume	Normalized Intake Valve Diameter	Normalized Radius of Curvature of the Intake Port
Standard plenum	1.00	1.00	1.00	1.00	1.00
V1 plenum	1.08	1.04	3.80	1.00	1.00
Standard plenum with G2 port	0.9	1.22	1.00	1.00	10.4

4.2.1. Steady Simulations: Computational Mesh

For the steady-flow simulations, a hybrid mesh, i.e., partially structured and unstructured, has been used. Figure 10 shows the computational mesh for the baseline configuration with a valve lift equal to 12 mm. Figure 10b shows a detail of both the structured mesh, used to discretize the cylinder volume below the intake valve, and the unstructured mesh, employed for the upper region, which is geometrically more complex. For all test cases, the minimum and maximum cell sizes are equal to 0.739 mm and 7.386 mm, respectively. Furthermore, the average cell size in the cylinder is 2.216 mm. To assess the grid resolution sensitivity, a finer mesh is also employed for the baseline configuration, with a minimum cell size equal to 0.5 mm and a maximum cell size equal to 5.0 mm. Table 4 summarizes the number of computational cells and nodes for each configuration.



(**a**) (**b**)

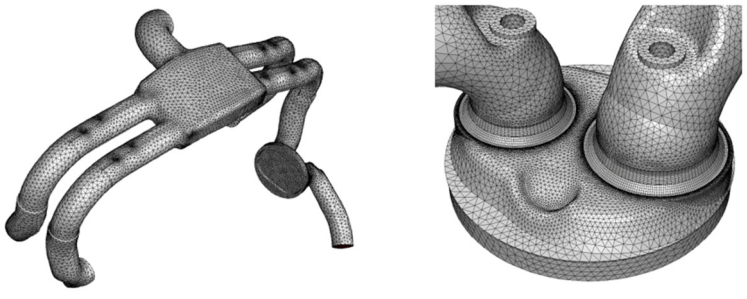
Figure 10. (**a**) Computational mesh for steady simulations. (**b**) Detail of the in-cylinder mesh along the intake valve axial plane.

Table 4. Mesh specifications for steady simulations.

	Coarse Mesh/Fine Mesh	
	Computational Cells	**Nodes**
Standard plenum	2,958,295/4,815,138	1,060,451/1,737,783
V1 plenum	4,056,245	1,426,729
Standard plenum with G2 port	3,148,286	1,135,218

4.2.2. Unsteady Simulations: Computational Mesh

The computational domain for the unsteady simulations includes the intake and exhaust valve motion and the piston motion. The geometry and the computational mesh at 323 CAD, i.e., before IVO, are shown in Figure 11 for the baseline configuration.



(**a**) (**b**)

Figure 11. Computational mesh for unsteady simulations: (**a**) unstructured tetrahedral grid for plenum, intake manifold, cylinder #1, and exhaust duct; (**b**) a detail of cylinder #1 at 323 CAD.

An unstructured mesh has been generated by setting the minimum and maximum sizes of the computational cells equal to 0.676 mm and 6.081 mm, respectively. The compu-

tational mesh has been refined near the intake and exhaust ports to increase the numerical accuracy. In the engine cylinder, the average numerical cell size is 3.041 mm with a growth rate equal to 1.2 to allow a smoother transition between regions of different surface and volume size. The computational mesh for the baseline configuration at 323 CAD consists of 1,043,629 cells and 311,814 nodes. The "dynamic mesh update method" has been employed in the simulations. At each time step, the re-meshing procedure has been applied based on the piston and valves motion. Three different mesh motion methods are employed to refresh the mesh in the deforming regions, i.e., a smoothing method, a dynamic layering method, and a local remeshing method. Specifically, for the intake and the exhaust valves lift, the dynamic layering method has been used to add or remove layers of cells adjacent to a moving boundary based on the height of the layer adjacent to the moving surface. The slip and collapse factors have been set to 0.2 and 0.4, respectively. A different approach has been used for the clearance and the swept volume. In the regions with triangular or tetrahedral meshes, the spring-based smoothing method has been employed. If the skewness or size criteria are not satisfied, the mesh is mainly re-generated in the regions close to the moving boundaries with a smoothing procedure applied to the distribution of the grid nodes, as shown in Figure 12. The same approach has been used for the other configurations. The numerical domain of the V1 plenum is discretized with 1,469,524 computational cells and 403,832 nodes at 323 CAD, whereas the baseline plenum with G2 port is discretized by 1,013,419 computational cells and 303,023 nodes at 323 CAD. A time step equal to 0.25 CAD has been used for all test cases.

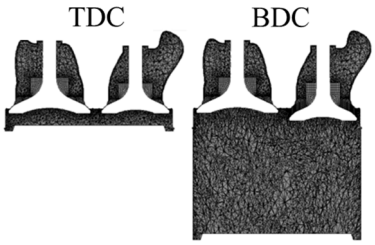
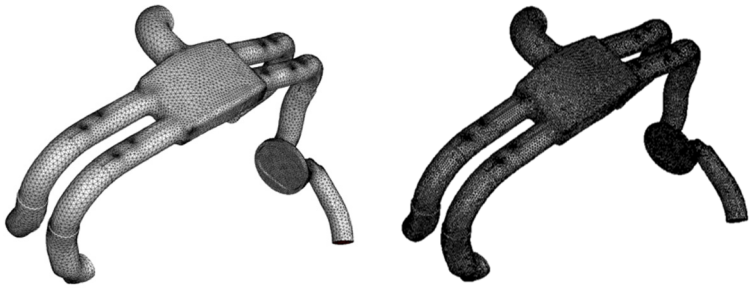


Figure 12. Dynamic remeshing of the computational grid on a crossing plane through the intake and exhaust valve axes (cylinder #1).

A grid refinement sensitivity analysis has also been carried out for the baseline plenum by employing a finer mesh with 2,433,378 computational cells and 717,063 nodes at 323 CAD. Figure 13a,b show the coarse and fine computational meshes, respectively.



(**a**) (**b**)

Figure 13. Computational mesh for unsteady simulations: (**a**) coarse and (**b**) fine refinement.

4.3. Initial and Boundary Conditions

For the steady-flow simulations, five valve lifts have been considered: 2.5 mm, 5 mm, 7.5 mm, 10 mm, and 12 mm. The inlet total temperature and total pressure, outlet static pressure, and wall temperature are set according to the measurements and are summarized in Table 5.

Table 5. Initial and boundary conditions for steady simulations.

Inlet Total Press. (bar)	Outlet Static Press. (bar)	Inlet Total Temp. (K)	Wall Temp. (K)
1.062	1.00	300.00	300.00

The unsteady simulations have been carried out by considering four different rpms, i.e., 2500, 5000, 5500, and 5800 rpm. For each case, the boundary and initial flow conditions are set according to the experimental data. The fresh air/fuel mixture pressure in the inlet section is equal to 0.980 bar, whereas the inlet gas temperature varies in the range 295.1–300.5 K, as shown in Table 6. The initial gas pressure in the cylinder is set to the experimental value at 323 CAD, whereas the initial gas temperature is set to 20 K higher than the gas temperature in the exhaust manifold. As regards wall temperatures, due to the lack of experimental data, reasonable values are set, as summarized in Table 7. The initial turbulent kinetic energy (k) and the initial rate of the dissipation of turbulent kinetic energy (ε) are given in Table 8.

Table 6. Initial and boundary conditions for unsteady simulations.

RPM	Initial CA (deg)	Final CA @ SA (deg)	Inlet Gas Mixture Temp. (K)	Inlet Gas Mixture Press. (bar)	Exhaust Gas Temp. (K)	Exhaust Gas Press. (bar)	Initial Gas Pressure in the Cylinder (bar)
2500	323.0	701.0	295.1	0.980	917.8	1.046	1.045
5000	323.0	689.0	298.4	0.980	1073.2	1.137	1.371
5500	323.0	689.0	299.7	0.980	1097.9	1.178	1.533
5800	323.0	689.0	300.5	0.980	1110.8	1.188	1.744

Table 7. Wall temperatures for unsteady simulations.

RPM	Plenum Wall Temperature (K)	Intake Valve Wall Temperature (K)	Exhaust Wall Temperature (K)	Exhaust Valve Wall Temperature (K)	Cylinder Wall (K)
2500	325	325	570	570	410
5000	317	317	585	585	410
5500	316	316	588	588	410
5800	315	315	590	590	410

Table 8. Initial turbulent parameters for unsteady simulations.

RPM	In-Cylinder TKE (m^2/s^2)	In-Cylinder Dissipation Rate (m^3/s^2)	TKE at Inlet and Outlet Sections (m^2/s^2)	ε at Inlet and Outlet Sections (m^3/s^2)
2500	1.60	230.4	0.40	144.0
5000	5.24	1404.0	0.70	110.0
5500	5.96	1677.0	0.76	113.0
5800	6.40	1843.0	0.80	115.0

5. Results and Discussion

Experiments and numerical simulations have been carried out to analyze the characteristics and the flow field during the intake process under both steady and unsteady conditions. Steady analysis aims to evaluate the intake valve discharge efficiency and the air volumetric flow rate through the valve for selected valve lifts. On the other hand, unsteady analysis is required to evaluate the volumetric efficiency of the engine and to study the flow field in the cylinder during the intake and compression strokes before combustion.

5.1. Model Validation and Flow Characterization Under Steady Conditions

The experimental and computed results under steady conditions are shown in Figure 14 for the baseline plenum, plenum V1, and G2 port, in terms of intake air volumetric flow

rate as a function of valve lift. The results show that the numerical simulations are in fair agreement with the experiments for all intake valve lifts. As expected, the volumetric flow rate increases with the valve lift until an asymptote is reached. For the baseline configuration and G2 port, the air volumetric flow rate reaches a maximum at a valve lift equal to 10 mm, which corresponds to the maximum value of the valve lift in the engine, as shown in Figure 3. On the other hand, for the V1 plenum, the asymptote has not yet been reached even with a valve lift of 12 mm. The figure shows that, at high valve lifts, i.e., 11 mm and 12 mm, the maximum volumetric flow rate belongs to the V1 plenum.

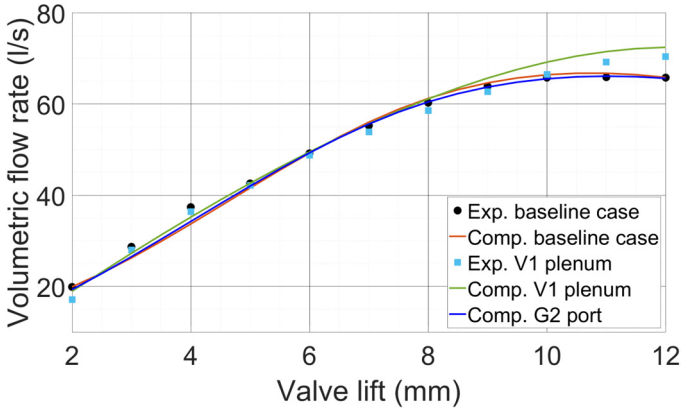


Figure 14. Intake volumetric flow rate as a function of valve lift.

Figure 15 compares the streamlines, the contour plots of velocity magnitude, and the velocity vectors on the intake valve axial plane at the maximum valve lift, i.e., 12 mm, for the three configurations. The contour plots of velocity magnitude show that the baseline case (standard plenum) and the standard plenum with the G2 port are characterized by higher gas velocities in the intake manifold than those reached with the V1 plenum configuration. In addition, Figure 15a–c show that, for all cases, the air flows through the valve opening and impinges on the cylinder liner splitting into two parts. The first part deflects along the cylinder axis direction, while the second part rotates towards the cylinder head, thus establishing a large recirculation region. As regards the region under the intake valve, a rotation of the flow streamlines occurs due to a concave profile (tulip type) of the valve head. Figure 16c shows the polar diagram of the gas velocity magnitude computed along the green circumference of Figure 16a,b. The polar diagram shows that the lowest gas velocities occur from 30 to 210 degrees (counterclockwise direction) due to either the small gap with the cylinder liner or the curvature of the intake manifold. In the same range, the velocity profiles are quite different depending on the geometry. On the other hand, the magnitude of the gas velocity is comparable in the range from 210 to 30 degrees for all configurations. The main conclusion is that, for steady simulations, the plenum geometry greatly affects the flow field inside the cylinder, and a larger plenum is beneficial to increase the intake volumetric flow rate.

For the baseline configuration and for three valve lifts, i.e., 5, 10, and 12 mm, a grid-refinement sensitivity analysis has been carried out to assess the accuracy of the numerical results. For instance, for the 12 mm valve lift case, the fine mesh consists of 4,815,138 computational cells and 1,737,783 nodes. The outcome of this analysis is given in Table 9 in terms of air volumetric flow rate. The percentage difference between measurements and numerical data is less than 1% for the finer mesh for all valve lifts, whereas, for 5 mm valve lift, the coarse mesh underpredicts the measured volumetric flow rate by 2.35%. Nevertheless, it can be concluded that the coarse mesh provides reasonable results for the highest valve lifts.

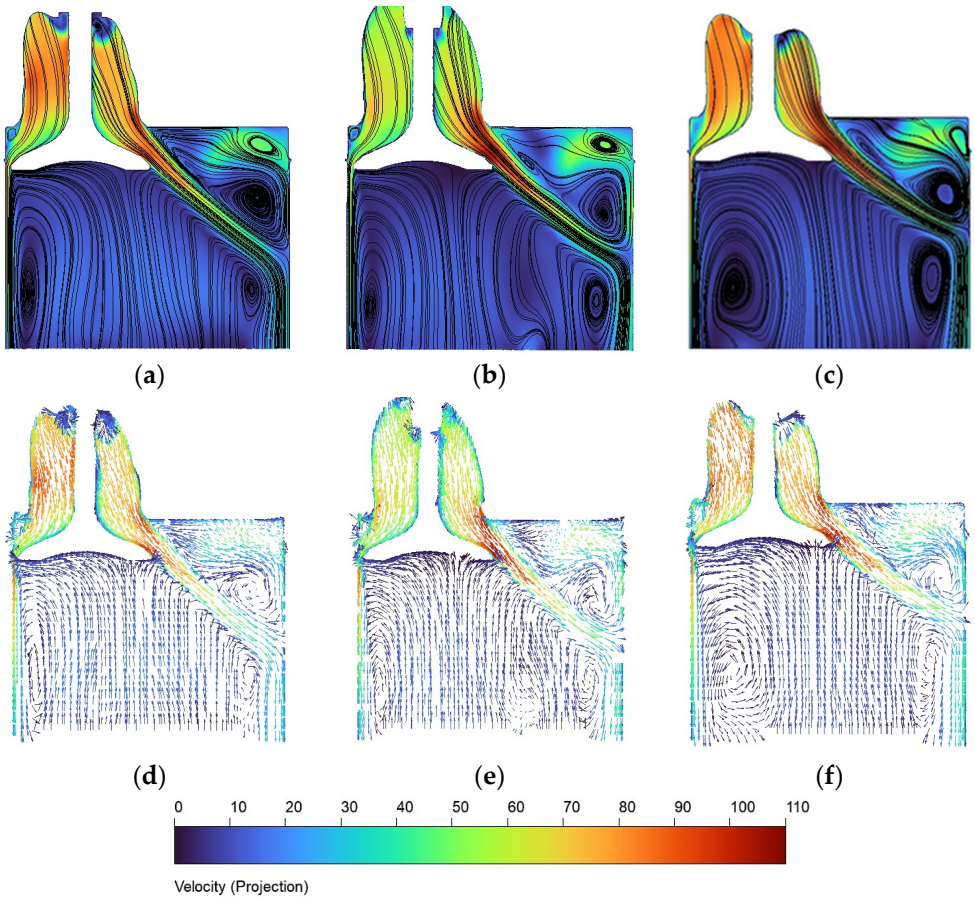


Figure 15. Streamlines and contour plots of velocity magnitude and velocity vectors on the intake valve axial plane with a valve lift of 12 mm: (**a**,**d**) baseline case; (**b**,**e**) V1 plenum; (**c**,**f**) standard plenum with G2 port.

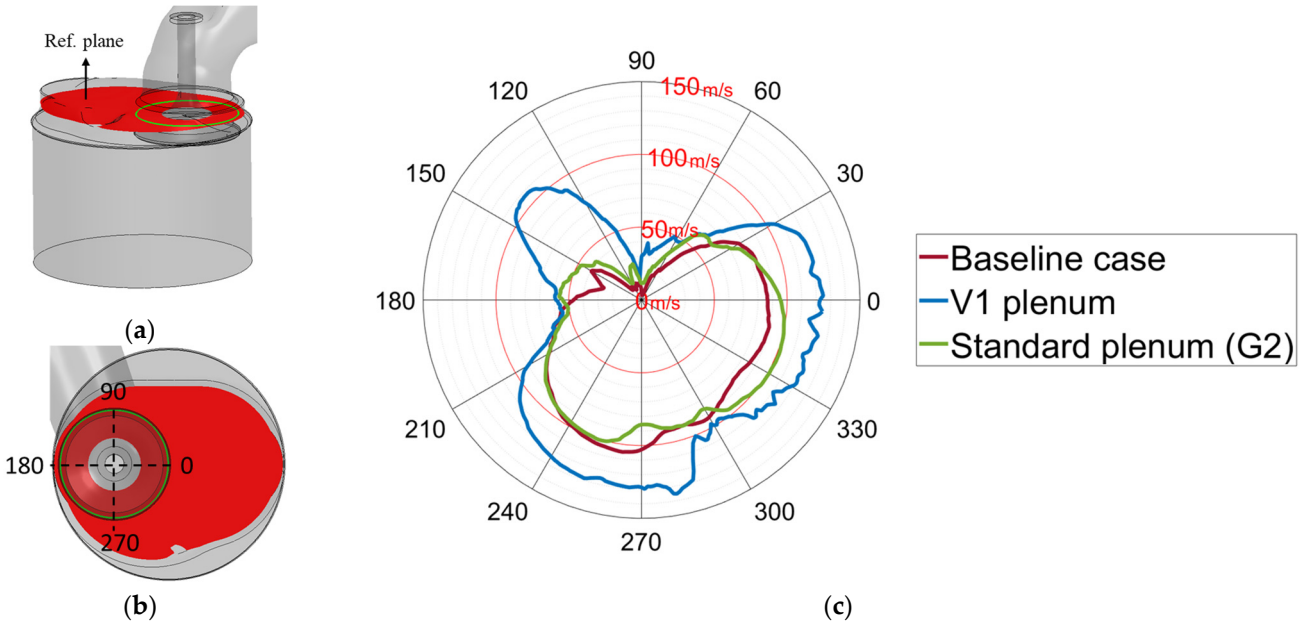


Figure 16. Front (**a**) and top (**b**) views of the half-way plane (red colored plane) with the curtain area (green circle) for a valve lift of 12 mm. Polar diagram (**c**) of gas velocity for baseline case (standard plenum), V1 plenum, and standard plenum with G2 port, along the green circle.

Table 9. Comparison between computed (with coarse and fine meshes) and experimental intake volumetric flow rate for different valve lifts.

		Fine Mesh		Coarse Mesh	
Valve Lift (mm)	**Exp. Data (L/s)**	**Volumetric Flow Rate (L/s)**	**Percentage Difference from Exp. Data**	**Volumetric Flow Rate (L/s)**	**Percentage Difference from Exp. Data**
5	42.6	42.4	−0.94%	41.6	−2.35%
10	65.8	66.0	+0.30%	66.4	+0.91%
12	65.8	65.4	−0.61%	66.4	+0.91%

5.2. Unsteady Simulations

Numerical simulations of the intake and compression strokes from IVO up to Spark Advance (SA) have been carried out for the baseline case by considering three different operating conditions corresponding to takeoff (5800 rpm), cruising (5000 rpm), and an intermediate regime (5500 rpm). The fresh charge and the residual gas trapped in the cylinder have been monitored to estimate the volumetric efficiency and to analyze the in-cylinder flow structure. Furthermore, the start-up regime (2500 rpm) has been considered to investigate the reverse flow from the cylinder towards the intake manifold. This reverse flow has been compared with that under takeoff condition. Finally, numerical simulations have been carried out to compare the volumetric efficiency of the intake process between the standard plenum and the other configurations under investigation.

5.2.1. Model Validation

The computational model has been validated by a comparison with experimental measurements for the baseline geometry. Three simulations have been carried out by considering the engine intake process at 5000, 5500, and 5800 rpm. The results have been compared in terms of in-cylinder pressure and volumetric efficiency. The initial flow field and the boundary conditions have been set according to the experimental values of Tables 6–8.

Figure 17 shows the comparison between the computed and the experimental volumetric efficiency. The computed volumetric efficiency (η_v) has been evaluated, given the trapped fresh charge mass ($m_{f.c.}$), the measured air/fuel ratio $(A/F)_{exp}$, the ambient air density (ρ_a), and the cylinder displacement (V_d), by means of the following expression:

$$\eta_v = \frac{m_{f.c.}}{\left[1+\frac{1}{(A/F)_{exp}}\right]} \Big/ \rho_a \cdot V_d \tag{7}$$

Figure 17 shows that the numerical model provides results that are in very good agreement with measurements. Moreover, the results show that the volumetric efficiency decreases by increasing rpm. The efficiency ranges from 0.897 at takeoff to 0.940 under cruising conditions. The computations and the measurements provide the same results, except at 5800 rpm, where the computed efficiency slightly overpredicts the measured volumetric efficiency. A grid refinement has been carried out, and the finer mesh in Figure 13 has been employed to get a more accurate prediction of the experimental data, as shown in Figure 17. The percentage difference with respect to the volumetric efficiency obtained by using the coarse mesh is 0.33%. Based on such a small percentage difference and to save computational time, the coarse mesh has been used for all the other simulations. Figure 18 shows a comparison between the measured and numerical results in terms of in-cylinder pressure for the three rpms. A good agreement is observed, with some discrepancies up to 450 CAD. Such differences are due to the assumptions in terms of initial distribution in the computational domain of the turbulence level, gas velocity, pressure, and temperature.

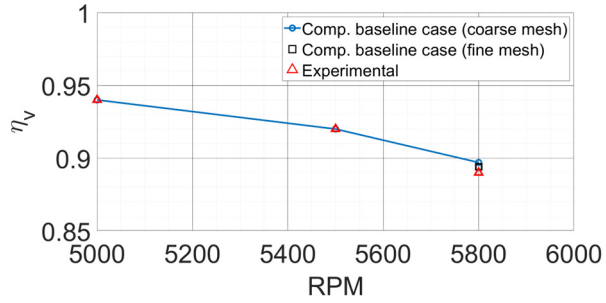


Figure 17. Experimental and numerical volumetric efficiency vs. rpm by using the baseline plenum.

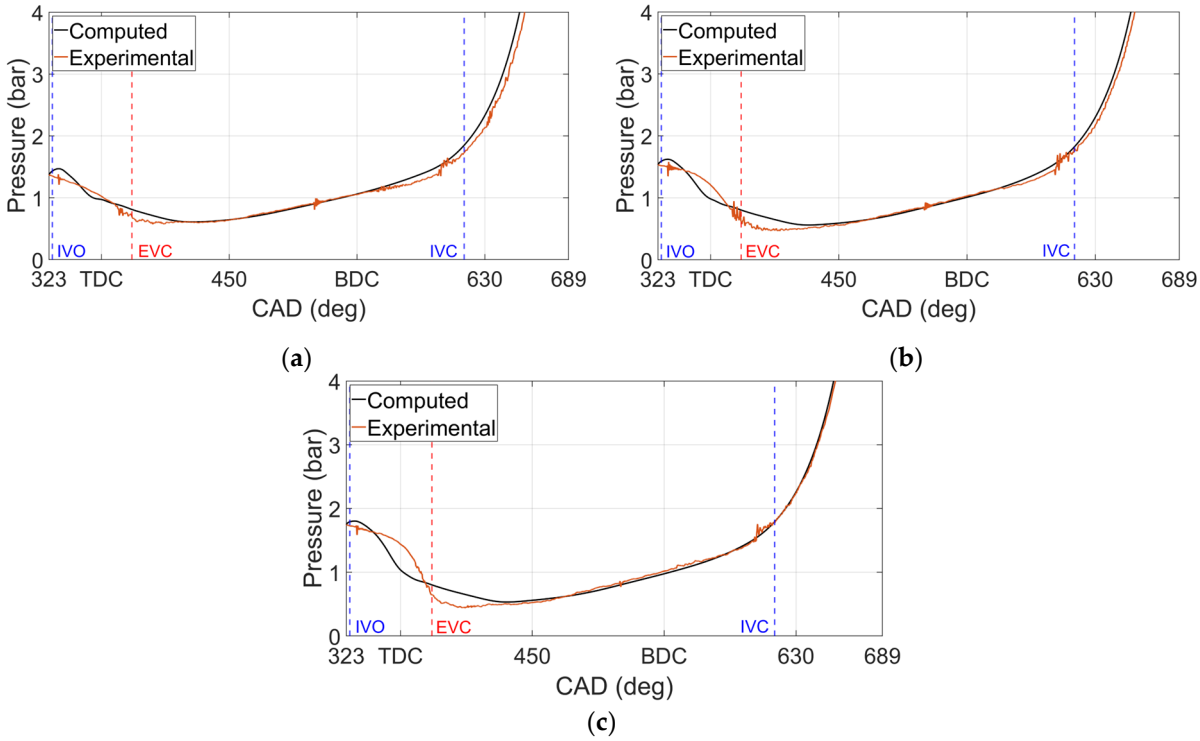


Figure 18. Experimental and numerical results in terms of in-cylinder pressure at 5000 rpm (**a**), 5500 rpm (**b**), and 5800 rpm (**c**) for the baseline plenum. Red dashed line indicates EVC; blue dashed lines indicate IVO and IVC.

5.2.2. The Intake Process with the Standard Plenum

The amount of residual gas in the combustion chamber is strongly influenced by the exhaust and intake processes and affects both the volumetric efficiency and the engine performance. The main parameters that affect the amount of residual gas mass are the intake, exhaust and cylinder pressures, engine speed, compression ratio, and valve timing. The reduction in such residual gas mass leads to an increase in the available cylinder volume for the fresh charge with a corresponding increase in the volumetric efficiency. The amount of residual gas is the result of two processes: the burned gas trapped in the cylinder before IVO and the back-flow of burned gas from the exhaust manifold to the cylinder during the valves' overlap period. A reverse flow may also occur from the cylinder towards the intake manifold due to inertial effects and to the pressure difference between the cylinder and the intake manifold. However, the burned gas in the intake manifold flows back into the cylinder during the intake stroke. Figure 19 shows the contour plots of the burned gas mass fraction during the overlap period (IVO to EVC) at 2500 rpm and 5800 rpm. The figure shows that the back-flow of the burned gas towards the intake manifold increases with the engine speed. Furthermore, at low engine speed, the fresh mixture starts to enter into the cylinder before the end of the overlap period.

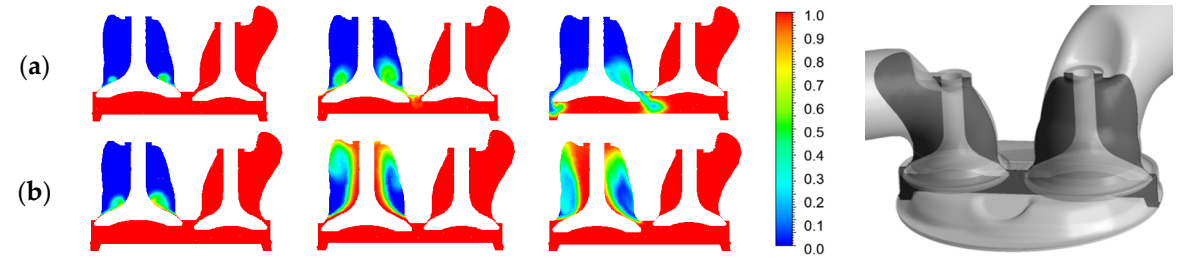


Figure 19. Contour plots of burned gas mass fraction at 2500 rpm (**a**) and 5800 rpm (**b**) along the valves axis plane. In the legend, 0 stands for fresh charge and 1 for residual gas mass fractions.

The in-cylinder total gas mass, the fresh charge mass and the residual gas mass as a function of CAD are shown in Figure 20 at 2500, 5000, 5500 and 5800 rpm, starting from IVO. During the first stage of the compression stroke (i.e., intake valve still open), the in-cylinder gas pressure starts to rise and a fraction of the fresh charge flows back to the intake manifold. This process is more pronounced at low engine speed. Table 10 gives the amount of fresh charge mass and residual gas mass in the cylinder at IVC and the mass percentage reduction of fresh charge due to back-flow through the intake port. With the exception of 2500 rpm, where reverse flow plays a major role, the results show that the amount of fresh charge trapped in the cylinder after IVC decreases as engine speed increases. An opposite trend has been observed for the residual gas mass. Furthermore, it is observed that the reverse flow starts later as the engine speed increases with a decrease in the back-flow mass percentage. Figure 20 confirms that both the intake and the exhaust valves lift and timing are selected to maximize the volumetric efficiency at the highest engine speeds. This is the best choice for aircraft applications.

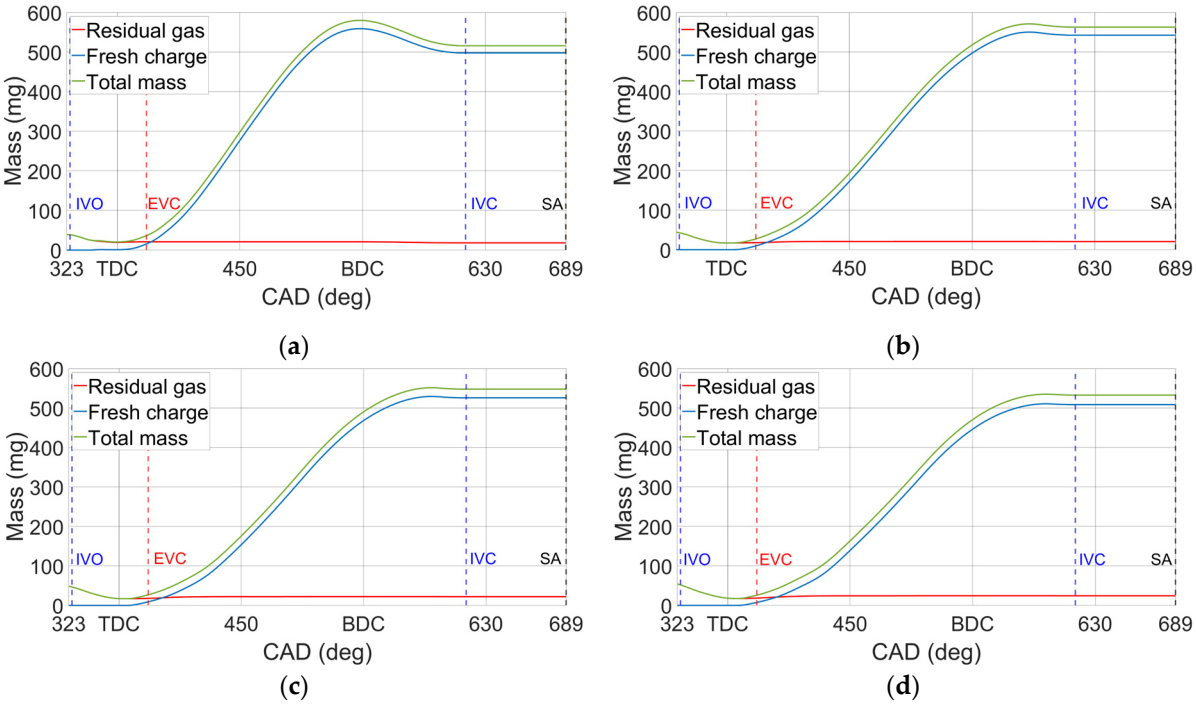


Figure 20. Computed in-cylinder fresh charge, residual gas, and total gas mass as a function of CAD at 2500 rpm (**a**), 5000 rpm (**b**), 5500 rpm (**c**), and 5800 rpm (**d**) with standard plenum. Red dashed line indicates EVC, blue dashed lines indicate IVO and IVC, and black dashed line indicates SA.

Table 10. In-cylinder fresh and residual gas mass at IVC, reverse flow starting time and mass percentage reduction due to reverse flow with the standard plenum.

RPM	Fresh Charge at IVC (mg)	Residual Gas at IVC (mg)	Reverse Flow	
			Starting Time (CAD)	Mass Reduction (%)
2500	497.70	20.90	538.0	10.97
5000	542.46	20.43	567.0	1.45
5500	525.85	21.97	578.5	0.65
5800	508.63	24.02	584.5	0.46

In order to better understand the reverse flow of the fresh charge, Figure 21 shows the computed gas pressure in the intake manifold (at the pressure probe location shown in Figure 1) and in the cylinder for 2500, 5000, 5500, and 5800 rpms. The results show that the gas pressure in the intake manifold is higher than the in-cylinder pressure for a long portion of the intake stroke. After BDC, the in-cylinder pressure rises due to the reduction in the cylinder volume and exceeds the intake gas pressure before IVC, thus leading to the reverse flow of the fresh charge from the cylinder to the intake manifold. However, at 2500 rpm, the in-cylinder pressure is higher than the intake pressure even before BDC, so the fresh charge starts to decrease earlier than in higher rpm cases, as shown in Figure 20.

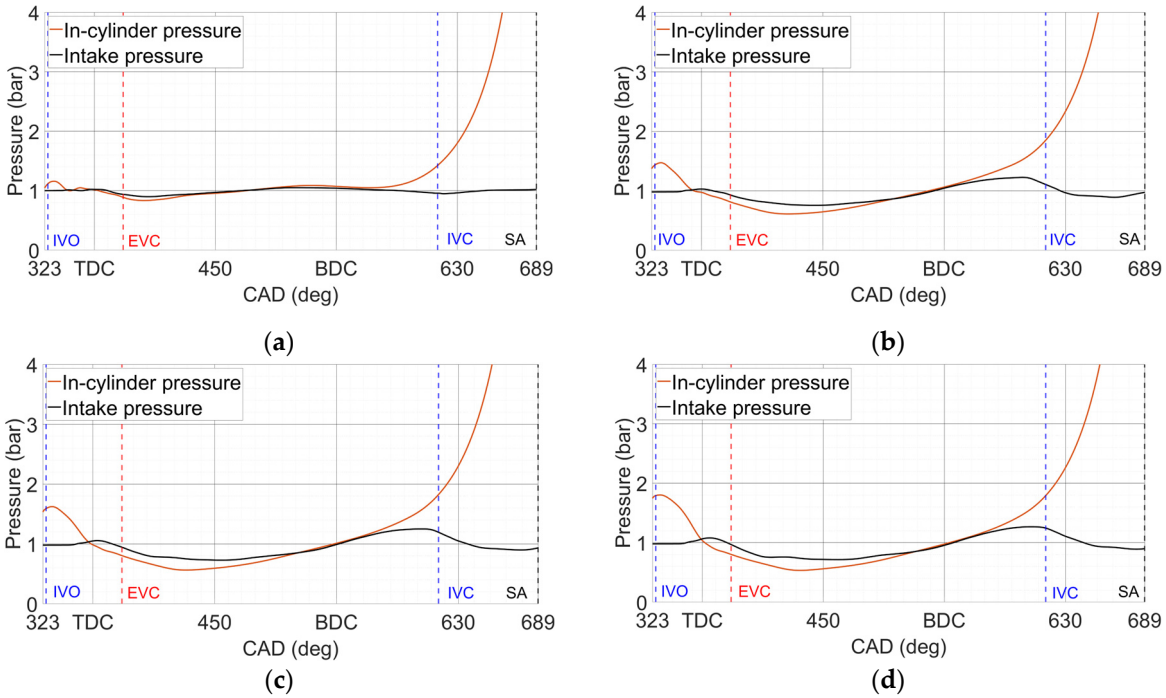


Figure 21. Computed gas pressure in the intake manifold and in the cylinder vs. CAD at different rpms with the baseline plenum: (**a**) 2500 rpm, (**b**) 5000 rpm, (**c**) 5500 rpm, and (**d**) 5800 rpm. Red dashed line indicates EVC, blue dashed lines indicate IVO and IVC, and black dashed line indicates SA.

5.2.3. The Influence of the Plenum Geometry

A new geometry of the intake system, namely, the V1 plenum (Figure 8), has been considered for comparison with the standard plenum. The numerical simulations for this geometry have been carried out with the same boundary and initial flow conditions of the standard plenum (Tables 6–8). The numerical profiles of the in-cylinder total gas mass for the baseline case and V1 plenum as a function of CAD are given for comparison in Figure 22 at 5000, 5500, and 5800 rpm. At all rpms, although the intake system equipped with the

V1 plenum provides more fresh charge in the cylinder from EVC to BDC, the trapped fresh charge mass at IVC is lower than that with the standard plenum. The reduction in the in-cylinder mass due to the reverse flow through the intake port before IVC is observed for both plenums. However, the mass percentage reduction due to reverse flow with the V1 plenum is higher than that with the standard plenum and decreases as the engine speed increases. This is evident from Table 11, which summarizes the results of the numerical analysis with the V1 plenum. In addition, Table 11 also shows that the reverse flow process starts at the same CAD for all engine rpms. Finally, Figure 22 shows that as engine speed increases, the difference in terms of in-cylinder total mass between the two plenums decreases. Overall, the higher reverse flow together and the lower amount of fresh charge trapped in the cylinder suggest that the V1 plenum should result in lower volumetric efficiency than the baseline configuration.

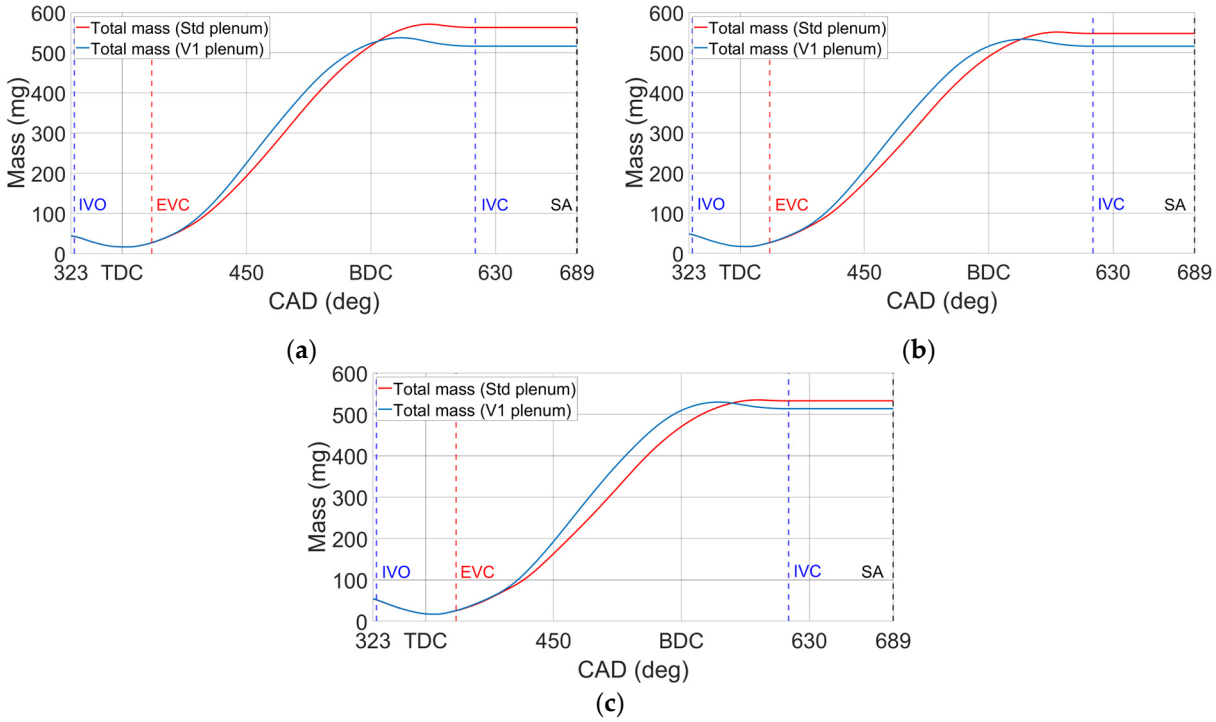


Figure 22. Numerical profiles of in-cylinder total gas mass as a function of CAD at 5000 rpm (**a**), 5500 rpm (**b**), and 5800 rpm (**c**) with standard plenum and V1 plenum. Red dashed line indicates EVC, blue dashed lines indicate IVO and IVC, and black dashed line indicates SA.

The computed volumetric efficiencies for both the standard plenum and V1 plenum, at 5000 rpm, 5500 rpm, and 5800 rpm, are compared in Table 12. The results show that, as expected, the standard plenum provides a higher volumetric efficiency with respect to the V1 plenum for all rpms. This is in agreement with the results in ref. [35], where a lower torque is observed with a larger plenum for engine speed up to about 7000 rpm. Moreover, with the V1 plenum, the volumetric efficiency is the same irrespective of the engine speed. The larger volume of the V1 plenum strongly influences pressure fluctuations both in the plenum itself and in the intake manifold. For instance, Figure 23 compares the computed gas pressure in both plenums during the engine intake process and compression stroke. The figure shows a smoother pressure profile for the V1 plenum from EVC to BDC. This is because the larger V1 plenum dampens the pressure waves more than the standard plenum does. From BDC to IVC, the pressure in the standard plenum is higher than that in the V1 plenum, so the highest volumetric efficiency occurs for the case with the highest pressure in the plenum before IVC, which is in agreement with other works in the literature [35,36].

Table 11. In-cylinder fresh and residual gas mass at IVC, reverse flow starting time and mass percentage reduction due to reverse flow with the V1 plenum.

RPM	Fresh Charge at IVC (mg)	Residual Gas at IVC (mg)	Reverse Flow	
			Starting Time (CAD)	Mass Reduction (%)
5000	496.34	19.99	566.0	3.84
5500	494.79	21.33	566.0	3.23
5800	490.33	23.64	566.0	2.95

Table 12. Comparison between the computed volumetric efficiency for the standard plenum and V1 plenum at 5000 rpm, 5500 rpm, and 5800 rpm.

RPM	η_v (Standard Plenum)	η_v (V1 Plenum)
5000	0.940	0.866
5500	0.920	0.867
5800	0.897	0.865

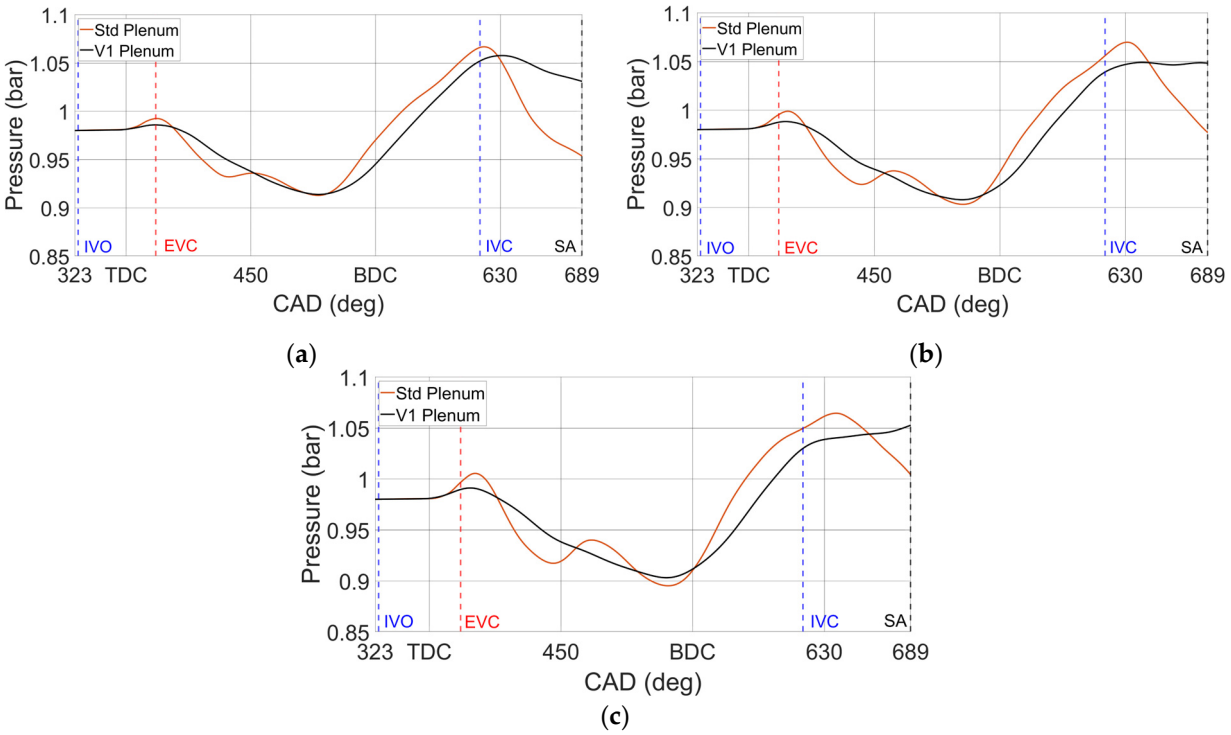


Figure 23. Computed gas pressure in the standard plenum and V1 plenum at 5000 rpm (**a**), 5500 rpm (**b**), and 5800 rpm (**c**). Red dashed line indicates EVC, blue dashed lines indicate IVO and IVC, and black dashed line indicates SA.

Figure 24 shows the difference in terms of computed gas pressure at the probe location in the intake manifold for the baseline case and the V1 plenum. The results show that, before BDC, the gas pressure for the baseline case is lower than that of the V1 plenum, and then after BDC it rapidly increases, leading to an increase in the fresh charge mass and in the volumetric efficiency. As regards the V1 plenum, the gas pressure increase is lower, and it drops at IVC, thus resulting in the reverse flow.

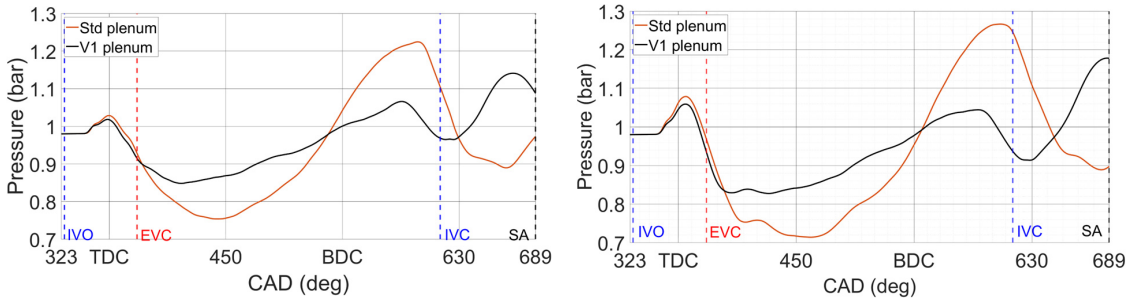


Figure 24. Computed gas pressure at the probe location for the baseline case and V1 plenum at 5000 rpm (**a**) and 5800 rpm (**b**). Red dashed line indicates EVC, blue dashed lines indicate IVO and IVC, and black dashed line indicates SA.

Figure 25 shows the in-cylinder TKE as a function of CAD for both baseline and V1 plenums during the four-stroke cycle under motored conditions. For both cases, the TKE increases after EVC, even if a lower TKE peak is observed for the V1 plenum. Then, the TKE is gradually dissipated for both cases, and the V1 plenum shows a lower value of TKE at SA. This may cause a lower flame speed during the combustion process.

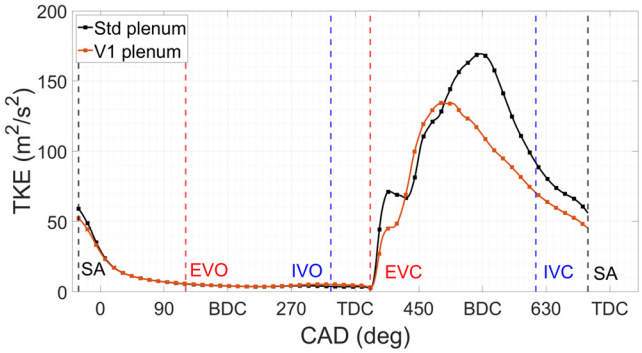


Figure 25. Turbulent kinetic energy in the chamber as a function of crank angle for the standard plenum and V1 plenum.

Finally, Figure 26 shows swirl and tumble ratios as a function of CAD for both the baseline case and the V1 plenum. The tumble ratio shows the same trend for both geometries up to EVC. After EVC, the tumble ratio increases, and a higher peak is reached for the V1 plenum case. Then, tumble motion is gradually dissipated, and, at IVC, the tumble ratio is lower for the V1 plenum than that of the baseline geometry. Additionally, based on the absolute value of the swirl ratio, Figure 26 shows that, at SA, the V1 plenum is characterized by a lower swirl intensity than the baseline case.

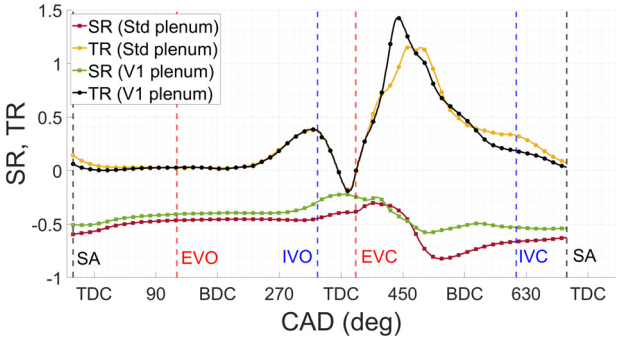


Figure 26. Mass-average swirl ratio (SR) and tumble ratio (TR) as a function of crank angle for standard plenum and V1 plenum.

5.2.4. The Influence of the Intake Manifold Geometry

A new intake manifold, namely, the G2 port, with a larger radius of curvature with respect to the baseline case, is also investigated (Figure 9b). It is believed that such a new manifold will decrease the flow resistance and minimize the pressure drop due to the flow deflection. The numerical simulations with the new intake manifold are carried out at 5800 rpm with the same initial and boundary conditions of the standard plenum (Tables 6–8).

Figure 27 shows the total mass trapped in the cylinder, the fresh charge, and the residual gas as a function of CAD. Table 13 summarizes the results for both the baseline case and the standard plenum with the G2 port. The use of the standard plenum with the G2 port increases the amount of fresh charge in the chamber and, consequently, the volumetric efficiency with respect to the baseline case.

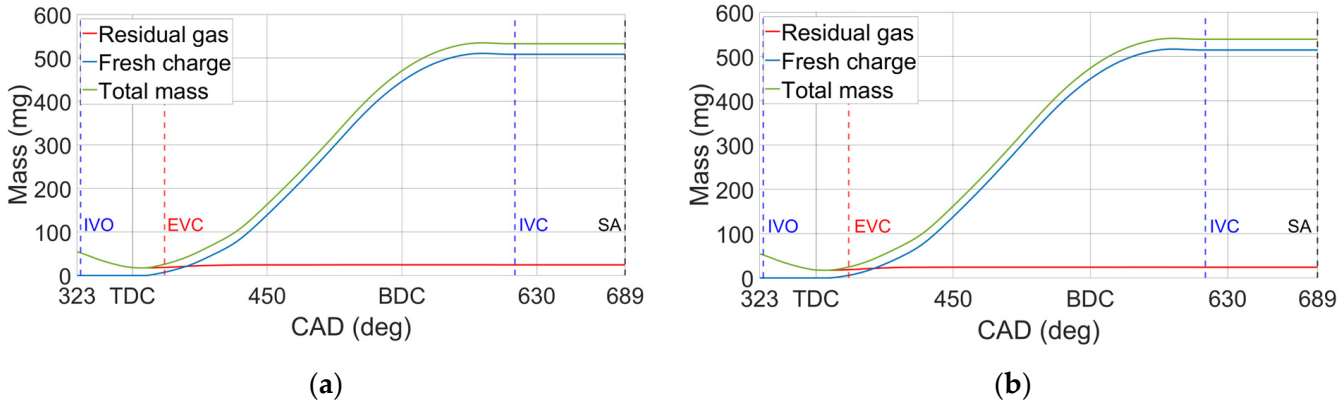


Figure 27. Computed in-cylinder fresh charge, residual gas, and total gas mass as a function of CAD at 5800 rpm for (**a**) the baseline case and (**b**) the standard plenum with G2 port. Red dashed line indicates EVC, blue dashed lines indicate IVO and IVC, and black dashed line indicates SA.

Table 13. In-cylinder fresh and residual gas mass at IVC, reverse flow starting time, mass percentage reduction due to of reverse flow, and volumetric efficiency for baseline case and standard plenum with G2 port at 5800 rpm.

	Fresh Charge at IVC (mg)	Residual Gas at IVC (mg)	Reverse Flow Starting Time (CAD)	Mass Reduction Due to Reverse Flow (%)	Volumetric Efficiency
Baseline case	508.63	24.02	584.5	0.46	0.897
Std. plenum with G2 port	514.91	24.19	594.5	0.39	0.910

On the other hand, the standard plenum with the G2 port does not modify significantly the amount of residual gas trapped in the cylinder with respect to the baseline case. Moreover, the reverse flow process starts approximately 10 CAD later than the baseline case with a lower mass percentage of back-flow.

Figure 28 shows a comparison between the baseline case and the standard plenum with the G2 port in terms of the TKE in the cylinder as a function of CAD for the four-stroke cycle under motored conditions. The TKE increases starting from EVC, reaching a maximum near BDC for both cases. The baseline case shows a higher and later TKE peak than the intake system equipped with the G2 port. After BDC, the TKE is gradually dissipated for both geometries. Finally, at SA, the values of the TKE are comparable for both cases.

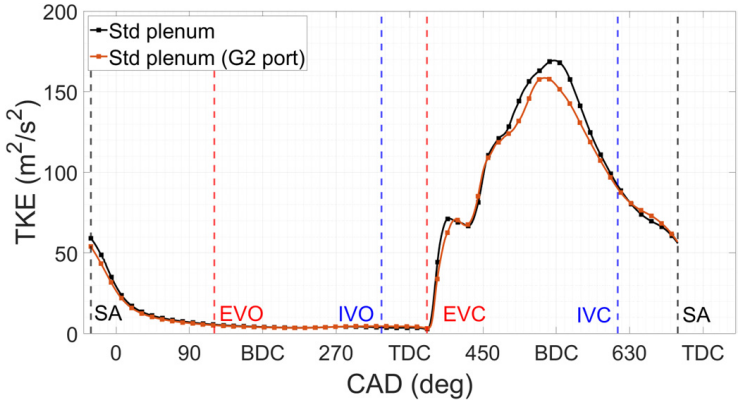


Figure 28. Turbulent kinetic energy in the engine chamber as a function of crank angle for the baseline case and standard plenum with G2 port.

Finally, Figure 29 shows the swirl and tumble ratios as a function of CAD for the baseline case and the standard plenum with the G2 port. The results show that the tumble ratios are comparable for both geometries until EVC. During the intake process, the baseline case shows a higher peak but a more rapid dissipation after that, which leads to a lower value at IVC. As regards the swirl ratio, a different behavior is observed with respect to the comparison between the baseline case and the standard plenum with the G2 port. Indeed, the absolute value of the swirl ratio of the baseline case is lower than that of the standard plenum with the G2 port, except for a short period during the intake process, where swirl ratios are comparable.

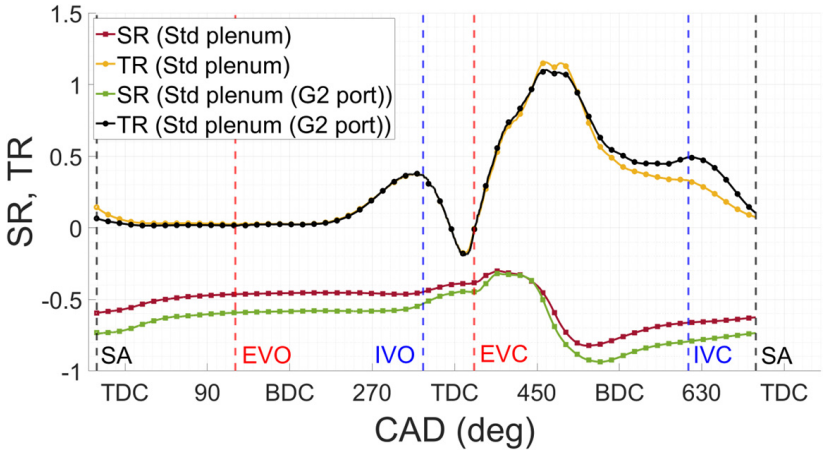


Figure 29. Mass-average swirl ratio (SR) and tumble ratio (TR) as a function of crank angle of the baseline case and standard plenum with G2 port.

6. Conclusions

This work aims to investigate the influence of plenum and port geometry on the engine performance, in terms of volumetric efficiency, turbulence intensity, and trapped fresh charge in the cylinder, of a naturally aspirated four-stroke spark ignition engine for ultralight aircraft applications. Three different geometries of the intake system, i.e., standard plenum (baseline case), V1 plenum (a larger volume of the plenum), and standard plenum with a G2 port (intake manifold with a larger curvature radius), are proposed. Several experiments and numerical tests, under both steady and unsteady conditions, have been carried out. Specifically, for unsteady conditions, the start-up (2500 rpm), cruising (5000 rpm), take-off (5800 rpm), and intermediate (5500 rpm) regimes have been investigated. The main results can be summarized as follows:

1. The steady-state simulations are able to accurately reproduce the measured intake air mass flow rate. Additionally, the simulations show that the V1 plenum is characterized by a higher mass flow rate through the curtain section of the intake valve than the other geometries;
2. Under steady flow, the optimum intake valve lift is equal to 10 mm for the baseline case. Furthermore, the results show that the V1 plenum is characterized by a higher air mass flow rate than the other geometries for high valve lifts up to 12 mm. At the maximum valve lift, the V1 plenum allows an increase in air mass flow rate of 9.1% and 9.4% compared to the standard plenum and the standard plenum with the G2 port, respectively;
3. Experimental tests under unsteady conditions have been carried out to estimate the volumetric efficiency for the standard plenum. The results show that the measured volumetric efficiency reaches a maximum value of 0.94 at 5000 rpm. A slight reduction in the volumetric efficiency has been observed by increasing the engine speed, i.e., 0.92 and 0.89 at 5500 rpm and 5800 rpm, respectively;
4. The unsteady numerical simulations, by using the RNG k-ε model with compressibility effects, are able to reproduce the experimental results with a good accuracy for the standard plenum. Therefore, the numerical model has been used to investigate the influence of the intake system geometry on the engine performance;
5. The V1 plenum geometry reduces the volumetric efficiency with respect to the baseline case. Specifically, a reduction of 7.87%, 5.76%, and 3.57% in terms of volumetric efficiency has been observed at 5000, 5500, and 5800 rpm, respectively. However, the larger volume allows us to dampen the pressure oscillations and to achieve less variations in terms of volumetric efficiency as the engine speed increases;
6. The standard plenum with the G2 port shows an increase of about 1.5% in terms of volumetric efficiency at 5800 rpm with respect to the baseline case;
7. TKE has been calculated for the three intake geometries for the four-stroke cycle under unfired conditions. The V1 plenum shows an advanced and lower peak of TKE than the other two geometries. The baseline case and the standard plenum with the G2 port show a higher TKE at SA than the V1 plenum. This is expected to enhance the flame propagation;
8. The in-cylinder flow field structure has been investigated for the three geometries during the intake and compression strokes. The standard plenum with the G2 intake port shows higher swirl and tumble ratios than the other geometries. This is expected to improve mixing and flame propagation.

Author Contributions: Conceptualization, A.V., P.C. and V.M.; methodology, F.A., F.F. and V.M.; software, F.A.; validation, F.A., D.S. and V.M.; investigation, A.V., P.C., D.S. and V.M.; resources, F.F., P.C. and V.M.; data curation, F.A. and D.S.; writing—original draft preparation, F.A., P.C. and D.S.; writing—review and editing, A.V., F.F. and V.M.; supervision, A.V., F.F., P.C. and V.M.; project administration, A.V., P.C. and V.M. All authors have read and agreed to the published version of the manuscript.

Funding: This research (grant number CDS_00595) was funded by MISE "Ministero dello Sviluppo Economico" and MUR "Ministero dell'Università e della Ricerca" under Project SIMPA "Sistemi Innovativi per Motori a Pistoni Aeronautici", Asse I, Priorità di Investimento 1.b, Azione 1.1.3 LDR.

Data Availability Statement: The original contributions presented in the study are included in the article; further inquiries can be directed to the corresponding author.

Conflicts of Interest: Fabio Anaclerio, Annarita Viggiano, Francesco Fornarelli, and Vinicio Magi declare no conflicts of interest. Paolo Caso and Domenico Sparaco are employees of the company Costruzioni Motori Diesel S.p.a. The funders had no role in the design of the study; in the collection, analyses, or interpretation of data; in the writing of the manuscript; or in the decision to publish the results.

References

1. Heywood, J.B. *Internal Combustion Engine Fundamentals*; McGraw-Hill: New York, NY, USA, 1988.
2. Yee, V.F.; Perry, S.; Jaromìr Klemes, J.; Tin Lee, C. A review on air emissions assessment: Transportation. *J. Clean. Prod.* **2018**, *194*, 673–684.
3. Climate Change and Flying: What Share of Global CO_2 Emissions Come from Aviation? Available online: https://ourworldindata.org/co2-emissions-from-aviation (accessed on 17 September 2024).
4. Air Pollutant Emissions Worldwide from 2015 to 2050, by Compound. 2020. Available online: https://www.statista.com/statistics/1014091/air-pollutants-emissions-worldwide-by-compound/ (accessed on 17 September 2024).
5. CO_2 Emissions in 2023, A New Record High, but Is There Light at the End of the Tunnel? Available online: https://iea.blob.core.windows.net/assets/33e2badc-b839-4c18-84ce-f6387b3c008f/CO2Emissionsin2023.pdf (accessed on 9 October 2024).
6. European Commission. Directive 2015/1513 of the European Parliament and of the Council amending Directive 98/70/EC relating to the quality of petrol and diesel fuels and amending Directive 2009/28/EC on the promotion of the use of energy from renewable sources. *Off. J. Eur. Union* **2015**, *239*, 1–29.
7. Liobikienė, G.; Butkus, M. The European Union possibilities to achieve targets of Europe 2020 and Paris agreement climate policy. *Renew. Energy* **2017**, *106*, 298–309. [CrossRef]
8. Mørch, C.S.; Bjerre, A.; Gøttrup, M.P.; Sorenson, S.C.; Schramm, J. Ammonia/hydrogen mixtures in an SI-engine: Engine performance and analysis of a proposed fuel system. *Fuel* **2011**, *90*, 854–864. [CrossRef]
9. Purayl, S.T.P.; Hamdan, M.O.; Al-Omari, S.A.B.; Selim, M.Y.E.; Elnajjar, E. Review of hydrogen-gasoline SI dual fuel engines: Engine performance and emission. *Energy Rep.* **2023**, *9*, 4547–4573. [CrossRef]
10. Dimitriou, P.; Tsujimura, T. A review of hydrogen as a compression ignition engine fuel. *Int. J. Hydrogen Energy* **2017**, *42*, 24470–24486. [CrossRef]
11. Wouters, C.; Burkardt, P.; Steeger, F.; Fleischmann, M.; Pischinger, S. Comprehensive assessment of methanol as an alternative fuel for spark-ignition engines. *Fuel* **2023**, *340*, 127627. [CrossRef]
12. D'Amato, M.; Magi, V.; Viggiano, A. On Iso-octane Combustion with Ozone Addition under HCCI Engine-Like Conditions. *J. Phys. Conf. Ser.* **2022**, *2385*, 012086. [CrossRef]
13. Kobashi, Y.; Dan Dan Da, T.; Inagaki, R.; Shibata, G.; Ogawa, H. Optimization of gasoline compression ignition combustion with ozone addition and two-stage direct-injection at middle loads. *IJER* **2021**, *23*, 1–11. [CrossRef]
14. Hong, C.; Ji, C.; Wang, S.; Xin, G.; Meng, H.; Yang, J.; Ma, T. An experimental study of a strategy to improve the combustion process of a hydrogen-blended ammonia engine under lean and WOT conditions. *Int. J. Hydrogen Energy* **2023**, *48*, 33719–33731. [CrossRef]
15. Yang, X.; Kuo, T.W.; Guralp, O.; Grover, R.O., Jr.; Najt, P. In-Cylinder Flow Correlations Between Steady Flow Bench and Motored Engine Using Computational Fluid Dynamics. *J. Eng. Gas Turbines Power* **2017**, *139*, 072802. [CrossRef]
16. Kiyota, Y.; Akishino, K.; Ando, H. Concept of Lean Combustion by Barrel-Stratification. *SAE Tech. Pap.* **1992**, *101*, 1333–1345.
17. Li, Y.; Zhao, H.; Leach, B.; Ma, T.; Ladommatos, N. Characterization of an in-cylinder flow structure in a high-tumble spark ignition engine. *Int. J. Engine Res.* **2004**, *5*, 375–400. [CrossRef]
18. Falfari, S.; Brusiani, F.; Bianchi, G.M. Assessment of the Influence of Intake Duct Geometrical Parameters on the Tumble Motion Generation in a Small Gasoline Engine. *SAE Int.* **2012**. [CrossRef]
19. Li, Z.; He, B.Q.; Zhao, H. Influences of intake ports and pent-roof structures on the flow characteristics of a poppet-valved two-stroke gasoline engine. *Int. J. Engine Res.* **2016**, *17*, 1077–1091. [CrossRef]
20. Wahono, B.; Setiawan, A.; Lim, O. Effect of the intake port flow direction on the stability and characteristics of the in-cylinder flow field of a small motorcycle engine. *Appl. Energy* **2021**, *288*, 116659. [CrossRef]
21. Lee, K.; Bae, C.; Kanh, K. The effects of tumble and swirl on flame propagation in a four-valve S.I. engine. *Appl. Therm. Eng.* **2017**, *27*, 2122–2130. [CrossRef]
22. Lippert, A.M.; El Tahry, S.H.; Huebler, M.S.; Parrish, S.E.; Inoue, H.; Noyori, T. Development and Optimization of a Small-Displacement Spark-Ignition Direct-Injection Engine—Full-Load Operation. *SAE Int.* **2004**. [CrossRef]
23. Benajes, J.; Reyes, E.; Galindo, J.; Peidro, J. Predesign Model for Intake Manifolds in Internal Combustion Engines. *SAE Tech. Pap.* **1997**. [CrossRef]
24. Silva, E.A.A.; Ochoa, A.A.V.; Henríquez, J.R. Analysis and runners length optimization of the intake manifold of a 4-cylinder spark ignition engine. *Energy Convers. Manag.* **2019**, *188*, 310–320. [CrossRef]
25. Siqueira Mazzaro, R.; de Hanriot, S.M.; Amorim, R.J.; Américo Almeida Magalhães Júnior, P. Numerical analysis of the air flow in internal combustion engine intake ducts Herschel-Quincke tubes. *Appl. Acoust.* **2020**, *165*, 107310. [CrossRef]
26. Ceviz, M.A.; Akin, M. Design of a new SI engine intake manifold with variable length plenum. *Energy Convers. Manag.* **2010**, *51*, 2239–2244. [CrossRef]
27. Harrison, M.F.; Dunkley, A. The acoustic of racing engine intake systems. *J. Sound Vib.* **2004**, *271*, 959–984. [CrossRef]
28. Oliveira, W.P.; Morais Hanriot, S.; Queiroz, J.M. Analysis of pulsating phenomena in an ICE intake manifold using lumped parameter and transfer matrix methods. *Appl. Acoust.* **2021**, *178*, 108029. [CrossRef]
29. Margary, R.; Nino, E.; Vafidis, C. The Effect of Intake Duct Length on the In-Cylinder Air Motion in a Motored Diesel Engine. *SAE Trans.* **1990**, *99*, 322–333.

30. Jemni, M.A.; Kantchev, G.; Abid, M.S. Influence of intake manifold design on in-cylinder flow and engine performances in a bus diesel engine converted to LPG gas fuelled, using CFD analyses and experimental investigations. *Energy* **2011**, *36*, 2701–2715. [CrossRef]
31. Manmadhachary, A.; Santosh Kumar, M.; Ravi Kumar, Y. Design&manufacturing of spiral intake manifold to improve Volument efficiency of injection diesel engine byAM process. *Mater. Today Proc.* **2017**, *4*, 1084–1090.
32. Costa, R.C.; Hanriot, S.M.; Sodré, J.R. Influence of intake pipe length and diameter on the performance of a spark ignition engine. *J. Braz. Soc. Mech. Sci. Eng.* **2014**, *36*, 29–35. [CrossRef]
33. Malkhede, D.; Khalane, H. Maximizing Volumetric Efficiency of IC Engine through Intake Manifold Tuning. *SAE Tech. Pap.* **2015**. [CrossRef]
34. Hamilton, L.J.; Lee, J.E. The Effects of Intake Plenum Volume on the Performance of a Small Normally Aspirated Restricted Engine. *SAE Int. J. Engines* **2009**, *1*, 1312–1318. [CrossRef]
35. Jawad, B.; Hoste, J.; Johnson, B. Formula SAE Dual Plenum Induction System Design. *SAE Tech. Pap.* **2002**. [CrossRef]
36. Ceviz, M.A. Intake plenum volume and its influence on the engine performance, cyclic variability and emissions. *Energy Convers. Manag.* **2007**, *48*, 961–966. [CrossRef]
37. Apaydin, S.; Doner, N. Simulation-based investigations of geometrical effects on the efficiency of the intake manifold of a six-cylinder diesel engine. *Adv. Eng. Softw.* **2022**, *173*, 103269. [CrossRef]
38. Pranoto, S.; Ubaidillah; Lenggana, B.W.; Budiana, E.P.; Wijayanta, A.T. Fluid Flow Analysis at Single and Dual Plenum Intake Manifolds to Reduce Pressure Drops Using Computational Approach. *J. Adv. Res. Fluid Mech. Therm. Sci.* **2022**, *97*, 1–12. [CrossRef]
39. *Formula SAE, Rules 2023*, 2nd ed.; SAE International: Warrendale, PA, USA, 2022.
40. Vichi, G.; Romani, L.; Ferrari, L.; Ferrara, G. Development of an Engine Variable Geometry Intake System for a Formula SAE Application. *Energy Procedia* **2015**, *81*, 930–941. [CrossRef]
41. Venugopal, T.; Anubhav, R. A New Approach for Development of a High-Performance Intake Manifold for a Single-Cylinder Engine Used in Formula SAE Application. *SAE Int. J. Engines* **2019**, *12*, 401–415. [CrossRef]
42. Scholz, P.; François, D.; Haubold, S.; Sun, S. WM-LES-Simulation of a Generic Intake Port Geometry. *SAE Int. J. Engines* **2018**, *11*, 331–348. [CrossRef]
43. Gong, C.; Sun, J.; Chen, Y.; Liu, F. Numerical study of cold-start performances of a medium compression ratio direct-injection twin-spark plug synchronous ignition engine fueled with methanol. *Fuel* **2021**, *285*, 119235. [CrossRef]
44. Wang, F.; Reitz, R.D.; Pera, C.; Wang, Z.; Wang, J. Application of Generalized RNG Turbulence Model to Flow in Motored Single-Cylinder PFI Engine. *Eng. Appl. Comput. Fluid Mech.* **2013**, *7*, 486–495. [CrossRef]
45. Da Costa, R.B.R.; Braga, R.M.; Gomes Júnior, C.A. PIV measurements and numerical analysis of in-cylinder tumble flow in a motored engine. *J. Braz. Soc. Mech. Sci. Eng.* **2017**, *39*, 3931–3945. [CrossRef]
46. Jamil, A.; Baharom, M.B.; Rashid, A.; Aziz, A. IC engine in-cylinder cold-flow analysis—A critical review. *Alex. Eng. J.* **2021**, *60*, 2921–2945. [CrossRef]

Disclaimer/Publisher's Note: The statements, opinions and data contained in all publications are solely those of the individual author(s) and contributor(s) and not of MDPI and/or the editor(s). MDPI and/or the editor(s) disclaim responsibility for any injury to people or property resulting from any ideas, methods, instructions or products referred to in the content.